

Seismic Characterizations of the Nisku Formation

Wabamun Area CO₂ Sequestration Project (WASP)

Authors

Abdullah Alshuhail

Don Lawton

Helen Isaac

Rev.	Date	Description	Prepared by
3	October 16, 2009	Final Draft	Abdullah Alshuhail, Don Lawton and Helen Isaac

Table of Contents

SUMMARY	9
1. Introduction	9
2. Data Calibration And Normalization	11
3. Regional Trend: 2d Seismic Data.....	15
4. Local Trends: 3d Seismic Data.....	19
5. Interpolation And Depth Conversion	26
6. Numerical Modelling	29
7. Seismic Attributes	34
8. Acoustic Impedance Inversion.....	40
9. Porosity Estimation	50
10. Rock Physics: Fluid Replacement Modelling	52
11. Conclusions	58
ACKNOWLEDGMENTS.....	59
REFERENCES.....	59

List of Tables

Table 1: Summary of available seismic and wireline data. HGFA refers to the WASP high-grade focus area.* Borehole data refers to both sonic log and Ireton top.	11
Table 2: Summary of some of the geological features within the multi-segment line (Figure 14).	25
Table 3: Comparison between the measured and estimated depth values using kriging algorithm (Figure 16). The difference between the two is also shown. The interpolation algorithm seems to honour the actual data, except at well 100163504701W500.	28
Table 4: Correlation coefficient (over a designed correlation window) between seismic data and synthetic seismogram from selected wells within the study area. The well locations are shown in the base map. The blue lines show the location of the 2D seismic (Figure 27) and the inline (Figure 30) invoked in the inversion.	42
Table 5: Parameters pertaining to the main constituents in the Gassmann FRM. The pressure, temperature, porosity and thickness of the Nisku Formation were 15 MPa, 50.3 Co, 9%, and 56 m respectively (Michael et al., 2008). Salinity and viscosity were adopted from Michael et al. (2008) whereas the rest of the parameters were calculated using the CREWES Fluid Property Calculator (Ursenbach, 2009) which is based on a paper by Batzle and Wang (1992) and the Peng-Robinson (1976) equation of state.	54

List of Figures

Figure 1: Base map showing the distribution of the seismic and borehole data. Cyan shapes indicate bodies of water.	10
Figure 2: Flowchart outlining the major steps followed in the seismic data calibration and normalization.	11
Figure 3: Seismic-to-well tie at the water source well (1F1-11-29-45-2W5). The location of the well and the seismic line (blue) are shown on the map. The correlation coefficient is 0.92 over the outlined zone (dashed rectangle) in the bottom image.	13
Figure 4: The 2D seismic line shown in Figure 3 with the synthetic track inserted at the well location (1F1-11-29-45-2W5). The seismic-to-well tie over the zone of interest enclosing the Nisku event (dashed rectangle) is enlarged in the bottom image.	14
Figure 5: Line 1 of the LITHOPROBE regional 2D seismic data with some of the major seismic events identified, including the Nisku. The location of Line 1 is shown by the blue line in the inset base map. The dashed arrow in the inset base map points to the location of a sudden change in the time structure (dashed rectangle), which could be associated with the Moon Lake reef boundary or simply a result of Line 1 turning into the updip direction. BH Lake is the Beaverhill Lake event.	15
Figure 6: Line 2 of the LITHOPROBE regional 2D seismic data with some of the major seismic events, identified including the Nisku. The location of Line 2 is shown by the blue line in the inset base map. The dashed arrow in the inset base map points to the location of the transition between the Nisku bank and Nisku shale basin (dashed rectangle). BH Lake is the Beaverhill Lake event.	16
Figure 7: Line 3 of the LITHOPROBE regional 2D seismic data with some of the major seismic events identified, including the Nisku. The location of Line 3 is shown by the blue line in the inset base map. The dashed arrow in the inset base map points to the location of the dashed ellipse, which marks a local anomaly interpreted to be caused by a discontinuity in the Wabamun event. BH Lake is the Beaverhill Lake event.	17
Figure 8: Line 4 of the LITHOPROBE regional 2D seismic data with some of the major seismic events identified, including the Nisku. The location of Line 4 is shown by the blue line in the inset base map. The dashed arrow in the inset base map points to the location of the dashed rectangle enclosing a local depression in the Wabamun event. BH Lake is the Beaverhill Lake event.	18
Figure 9: The time structure of the Nisku event after data calibration. The dashed black rectangle shows the extent of the zoom-in display over the study area in Figure 10.	20
Figure 10: Zoom-in display of the Nisku time structure map in Figure 9. The locations of some of the major anomalies are specified: Wabamun karsting (see Figure 14), Wabamun discontinuities, and the Nisku local time low. It should be emphasized that the karsting and discontinuity effects shown here are the footprints of those anomalies and do not indicate that the Nisku has been physically affected.	21
Figure 11: NRMS amplitude map of the Nisku event after data calibration and RMS amplitude normalization. Note the strong variations in the Nisku amplitude map compared to the time structure map. The dashed black rectangle shows the extent of the zoom-in display over the study area in Figure 12.	22

Figure 12: Zoom-in display of the Nisku NRMS amplitude map in Figure 11. Some of the major amplitude anomalies are specified: Wabamun karsting (see Figure 14), Wabamun discontinuities, and the Nisku amplitude low. It should be emphasized that the karsting and discontinuity effects shown here are the footprints of those anomalies and do not indicate that the Nisku has been physically affected..... 23

Figure 13: A multi-segment seismic section passing through some of the geological features within the reference 3D volume. The base map shows the location and orientation of the multi-segment section. The nodes are shown at their corresponding location along the horizontal axis. The right side of the colour scale in the base map represents the amplitude within the section (-3 to 3). The dashed rectangle indicates the extent of the zoom-in display in Figure 14. 24

Figure 14: A zoom-in display of the multi-segment line through the 3D volume in Figure 13. Segment 1-2 passes through the karsting (k) originating in the Wabamun event. Segments 2-3 and 3-4 cross local Wabamun discontinuities (d). Segments 4-5, 5-6, and 6-7 show an example of the Nisku amplitude changing from high (h) to low (l) to high (h) again. Note the broadening in the Nisku cycle in segment 5-6. Segment 7-8 shows some amplitude anomalies between 1150 and 1200 ms, which are interpreted to be associated with the Cretaceous strata. The change from moderate (m) to high (h) Nisku amplitude is illustrated in segment 8-9. Segment 8-9 also traverses an area of local Nisku amplitude thinning (t), which is mapped by the seismic attribute amplitude thickness of the peak (ATP). 25

Figure 15: Interpolated time structure map (Figure 9) using a kriging algorithm with a grid size of 50 × 50 m. 26

Figure 16: Interpolated depth structure map using a kriging algorithm with a grid size of 50 × 50 m. 27

Figure 17: Sequential display of the normal incidence synthetic seismogram in which the Nisku event amplitude is modelled as function of thickness and average P-wave velocity. The top of the Nisku event is identified as the peak at approximately 1130 ms (the green bracket along the time axis approximates the frequency cycle through the formation). In each blue bracket (thickness effect), there are 11 traces, each representing the seismic amplitude associated with that thickness and an average Nisku P-wave velocity increasing from 5500 m/s to 6500 m/s at an increment of 100 m/s. The modelling was undertaken using well 100-10-05-052-02W5. The actual Nisku thickness and average P-wave velocity at this well are 100 m and 6100 m/s, respectively..... 30

Figure 18: Nisku event amplitude (top) and time (bottom) as a function of thickness and average P-wave velocity. The actual Nisku thickness and average P-wave velocity are 100 m and 6100 m/s, respectively. The maps represent the Nisku amplitude and time horizons that resulted from picking the peak amplitude corresponding to the Nisku event in Figure 17. The black dashed rectangle outlines the most likely Nisku thickness and average velocity values within the study area based on well control. The results suggest that the Nisku average P-wave velocity (or impedance) effect is far more significant than the thickness effect. Thus, the highest sensitivity is along the vertical axis. 31

Figure 19: Nisku amplitude modelling result in which the difference between the thickness and average P-wave velocity effect on the Nisku event amplitude is evident. The actual Nisku thickness and average P-wave velocity are 100 m and 6100 m/s, respectively..... 32

Figure 20: Ireton event amplitude (top) and time (bottom) as a function of Nisku thickness and average P-wave velocity. The maps represent the Ireton amplitude and time horizons that resulted from picking the trough amplitude corresponding to the Ireton event in Figure 17. The black dashed rectangle outlines the most likely Nisku thickness and average P-wave velocity values within the study area based on well control. The results suggest that the effect of the Nisku average P-wave velocity (or impedance) footprint on the Ireton event is far more significant than the thickness effect. 33

Figure 21: Average NRMS Nisku amplitude over a 10 ms window (centred on the Nisku horizon pick). In addition to the patterns already defined in the NRMS Nisku amplitude map (Section 4 and Figure 12), another low amplitude pattern emerges from the map. The NRMS amplitude averaging window of 10 ms seems appropriate except within the north-eastern region of the easternmost 3D volume. The relative position to the large study area is shown by the dashed rectangle in the base map in Figure 11. 35

Figure 22: Amplitude thickness of the Nisku peak (ATP) in ms. The inset schematic illustrates the concept of ATP. Note the elongated (NE-SW) thinning pattern that is not captured by the NRMS amplitude map. See the multi-segment line in Figures 13 and 14 for a cross-sectional view of those anomalies. The relative position to the large study area is shown by the dashed rectangle in the base map in Figure 11. 36

Figure 23: Amplitude thickness of the Nisku peak (ATP in ms) of the synthetic seismogram in Figure 17. The ATP is highly sensitive to variations in the Nisku Formation thickness and average P-wave velocity over the expected range of those parameters. There is a distinct separation in the velocity effect over the expected Nisku Formation thickness (~ 40 – 80 m). The separation seems to be occurring around the tuning thickness (~ 60 m) and the corresponding average P-wave velocity (~ 6100 m/s). 37

Figure 24: Inline difference (coherency) attribute of the Nisku event in ms. The difference method shows more sensitivity toward discontinuities within the Nisku compared with other seismic attributes as can be seen, for instance, with the Wabamun karsting effect on the Nisku event. See the multi-segment line in Figures 13 and 14 for a cross-sectional view of some of the identified anomalies. The relative position to the large study area is shown by the dashed rectangle in the base map in Figure 11. 38

Figure 25: Crossline difference (coherency) attribute of the Nisku event in ms. Note the sensitivity, also, to the direction in which the difference is measured compared to the inline difference in Figure 24. The crossline difference was not as robust as the inline difference in defining geologic features within the reference 3D volume (e.g., the Wabamun karsting effect). However, it performed better in defining some of the features associated with other seismic volumes, such as the local time low (also shown in the time structure map in Figure 10). See the multi-segment line in (Figures 13 and 14) for a cross-sectional view of some of the identified anomalies. The relative position to the large study area is shown by the dashed rectangle in the base map in Figure 11. 39

Figure 26: Flowchart outlining the major steps followed in the seismic inversion to extract the acoustic impedance map of the Nisku event. 41

Figure 27: Seismic section near the water source well (Figure 3 and Table 4). The green curve at the well location is the correlated synthetic seismic trace. The correlation coefficient is 0.92. 43

Figure 28: The initial acoustic impedance model. The blue curve at the well location is the correlated synthetic seismic trace while the black curves are the actual seismic traces. 43

Figure 29: Estimated acoustic impedance along the 2D seismic line near the water source well (Figure 3) using band-limited (top) and model-based (bottom) inversion methods. The inserted blue curve at the well location represents the computed acoustic impedance from the sonic and density logs. The black curves represent the acoustic impedance from the band-limited inversion whereas in the model-based inversion they represent the misfit error..... 44

Figure 30: Inline extracted from the reference 3D seismic volume (Table 4). The green curve at the well location is the correlated synthetic seismic trace. The correlation coefficient is 0.80. 45

Figure 31: The initial acoustic impedance model corresponding to the inline in Figure 30. The blue curve at the well location is the correlated synthetic seismic trace while the black curves are the actual seismic traces..... 45

Figure 32: Estimated acoustic impedance of the inline in Figure 30 and Figure 31 using band-limited (top) and model-based (bottom) inversion methods. The inserted blue curve at the well location represents the computed acoustic impedance from the sonic and density logs. The black curves refer to the acoustic impedance from the band-limited inversion whereas in the model-based inversion they represent the misfit error..... 46

Figure 33: Estimated Acoustic impedance (I_p) map of the Nisku Formation using band-limited inversion. Due to lack of well control, the inversion was not performed on the entire dataset. The relative position to the large study area is shown by the dashed rectangle in the base map in Figure 11. 47

Figure 34: Estimated Acoustic impedance (I_p) map of the Nisku Formation using model-based inversion. Due to lack of well control, the inversion was not performed on the entire dataset. The relative position to the large study area is shown by the dashed rectangle in the base map in Figure 11. 48

Figure 35: Acoustic impedance (I_p) of the synthetic seismogram in Figure 17 using band-limited (top) and model-based (bottom) inversion methods. Similar to the seismic amplitude response, the acoustic impedance shows high sensitivity toward variations in the Nisku Formation average P-wave velocity rather than thickness. The maps illustrate the direct proportionality between average P-wave velocity and acoustic impedance. Note the similarity in the results except for the small difference in the magnitude of the acoustic impedance due to scaling issues. 49

Figure 36: Estimated bulk porosity of the Nisku event using Wylie’s time-average equation with bulk velocity derived from the band-limited acoustic impedance inversion. The relative position to the large study area is shown by the dashed rectangle in the base map in Figure 11..... 51

Figure 37: Predicted changes in the average acoustic (\bar{I}_p) and shear (\bar{I}_s) impedance of the Nisku Formation as a result of increasing the CO₂ saturation from 0 to 100%. The highest incremental change is associated with increasing the CO₂ saturation from 0 to 20%. Shortly after that, the acoustic impedance reaches a plateau. The shear impedance, on the other hand, is rather insensitive to the fluid replacement..... 55

Figure 38: Top left: Offset dependent synthetic seismogram generated using the Zoeppritz equations after NMO correction and stacking; all 11 traces are identical (in the base survey) and they represent an initial condition in which the reservoir is 100% brine saturated. Top right: the same offset dependent synthetics but in this case (monitor survey) each trace has undergone a saturation transformation between brine and CO₂ as indicated by the values along the horizontal axis (red label). Bottom: the difference between the monitor and base. Changes in reservoir properties were only applied to the zone of interest, i.e., Nisku (2238 m) to Ireton (2288 m). The highest incremental change is associated with the first 10% of CO₂ saturation (trace 2). The subtle difference between the two surveys suggests that the Nisku matrix is so stiff that the fluid replacement process is only having a small effect on the observed seismic response. The modelling was undertaken using the water source well (1F1-11-29-45-2W5). 56

Figure 39: Mosaic display of the fluid substitution effect on the time and amplitude response of the Nisku and Ireton events, respectively, between the base and monitor surveys: (a) difference in the Nisku event two-way time (ms); (b) difference in the Ireton event two-way time (ms); (c) difference in the Nisku event amplitude; (d) difference in the Ireton event amplitude. Each horizon is obtained by subtracting the corresponding horizons between the monitor and base surveys (difference = monitor - base) in Figure 38. In all the plots the highest incremental change in time and amplitude is associated with the initial increase in CO₂ saturation (i.e., from 0 to 10%). Shortly after that, the seismic response reaches a plateau and becomes virtually unresponsive to the increase in CO₂ saturation. The modelling was undertaken using the water source well (1F1-11-29-45-2W5) shown in Figure 3. 57

SUMMARY

Seismic characterization of the Nisku Formation in the Lake Wabamun area has revealed two primary groups of anomalies. The first group consists of anomalies interpreted to be footprints of geological discontinuities induced by dissolution in the overlying Wabamun Formation. Even though there is no evidence to indicate that the integrity of the Nisku Formation has been compromised, such geologic discontinuities should be taken into consideration if CO₂ were to be injected into the Nisku Formation. Regional 2D lines show no sign of faulting in the study area which might cause these observed discontinuities.

The second group of anomalies outlines contrasts in acoustic impedance caused by lateral changes in lithology and/or porosity of the Nisku Formation. This interpretation is constrained by well control and supported by seismic modelling, which suggests that changes in Nisku thickness over the range encountered in the study area has an insignificant effect on seismic amplitudes. If so, then seismic amplitude mapping may provide one approach in pursuing favourable sites for CO₂ injection in addition to acoustic impedance, which has rather limited implementation due to the scarcity of well control with appropriate log types and formation tops. In addition to the conventional time structure and amplitude maps, several seismic attributes were generated to further refine our interpretation of both geologic discontinuities and lithological variations of the Nisku Formation in the study area.

Our analysis revealed favourable low-impedance, high-porosity locations that could be potential injection sites. Finally, fluid replacement modelling was undertaken to predict the feasibility of time-lapse seismic monitoring for detecting an injected CO₂ plume. The results suggest that changes in seismic response will most likely be subtle and that the plume will probably be at the lower threshold of seismic detectability.

1. INTRODUCTION

Seismic characterization of the Nisku Formation in the Wabamun Area CO₂ Sequestration Project (WASP) high-grade focus area (HGFA) is based on analyzing and interpreting post-stack seismic datasets comprising more than two hundred 2D seismic lines and seven 3D volumes. The primary objectives were:

1. To map the Nisku Formation within the WASP high-grade focus area using available seismic data.
2. To delineate the seismic character of the Nisku Fm. (i.e., porosity/lithology indicators).
3. To identify geologic features that may compromise the Nisku Fm. caprock (e.g., anomalies and karsting).
4. To extract appropriate attributes from the seismic data for input into the static geological model.

The study area is surrounded by two major hydrocarbon resources in Alberta; the Leduc reef play (east) and the Moon Lake reef play (northwest). Thus, part of the study area was mapped using vintage surface seismic data that had been acquired as part of hydrocarbon exploration in the area. Table 1 gives an outline of the volume and approximate areal coverage of the analyzed seismic data as well as the number of wells with appropriate log curves and formation tops that were available for integration into the seismic data analysis. No new seismic data were acquired as part of Phase I of the project. The spatial distribution of the available seismic data is illustrated in Figure 1, and shows that the data coverage is not distributed uniformly. Thus characterization was constrained to

those areas with good coverage. The 2D seismic data were used primarily for identifying long-wavelength structures, whereas the high-quality 3D data were used for detailed mapping, inversion and generation of seismic attributes.

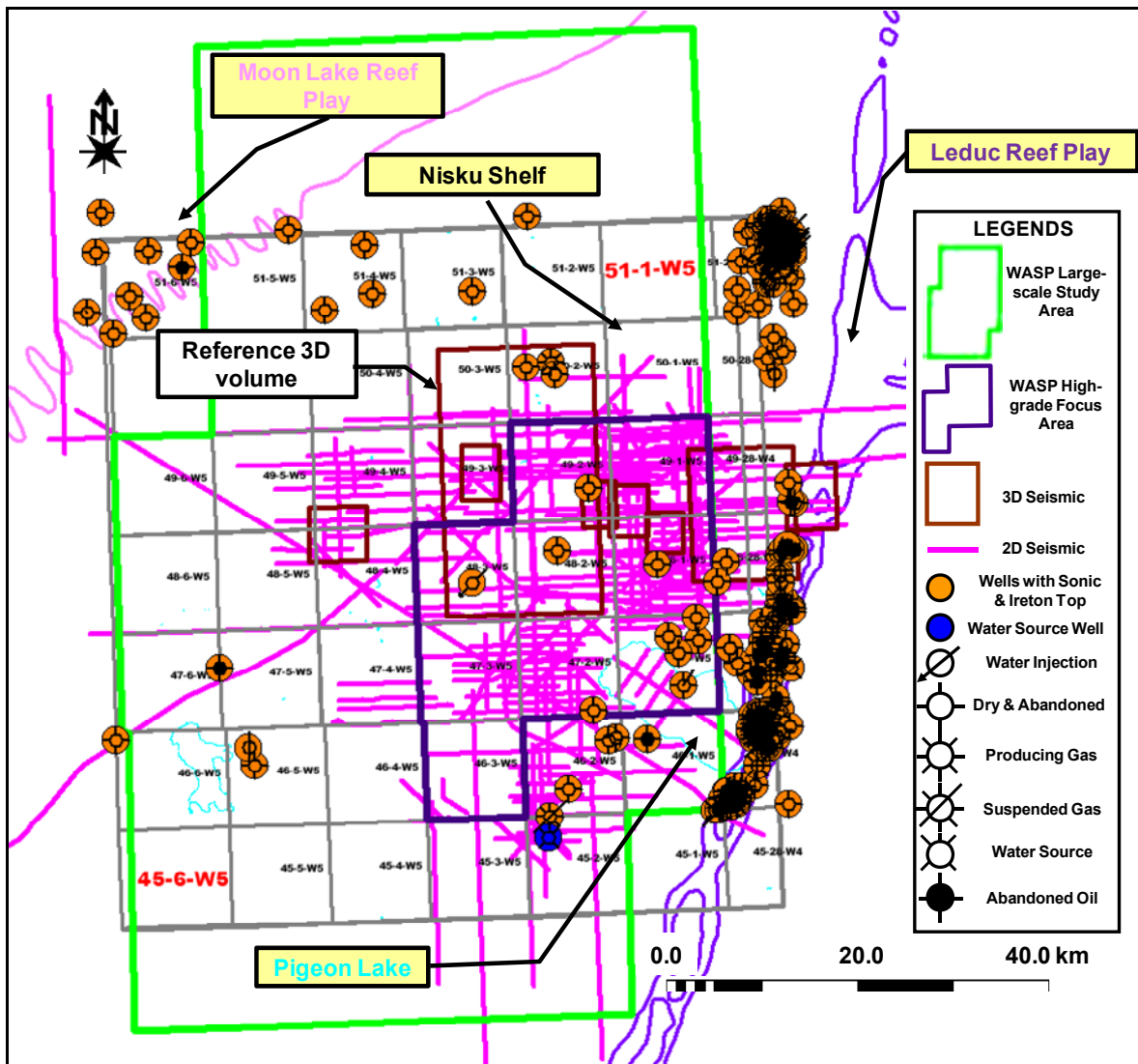


Figure 1: Base map showing the distribution of the seismic and borehole data. Cyan shapes indicate bodies of water.

Table 1: Summary of available seismic and wireline data. HGFA refers to the WASP high-grade focus area.* Borehole data refers to both sonic log and Ireton top.

Source	Data Type	Description
Seismic Data	2D	200 seismic lines, approximately 2,432 km in total length
	3D	7 seismic volumes covering an area of 419 km ²
Borehole Data*	Within HGFA	7 wells, only 2 coincide with seismic coverage
	Nearby HGFA	Over 15 wells, only 6 coincide with seismic coverage

2. DATA CALIBRATION AND NORMALIZATION

The 2D and 3D seismic datasets have different acquisition and processing specifications and were acquired over many years prior to this project being undertaken. Therefore, prior to interpretation, inversion and attribute analysis, two primary steps were undertaken: data calibration and amplitude normalization. These steps were necessary to account for the vintage and datum differences within the data. Figure 2 gives an overview of the data calibration and normalization approach.

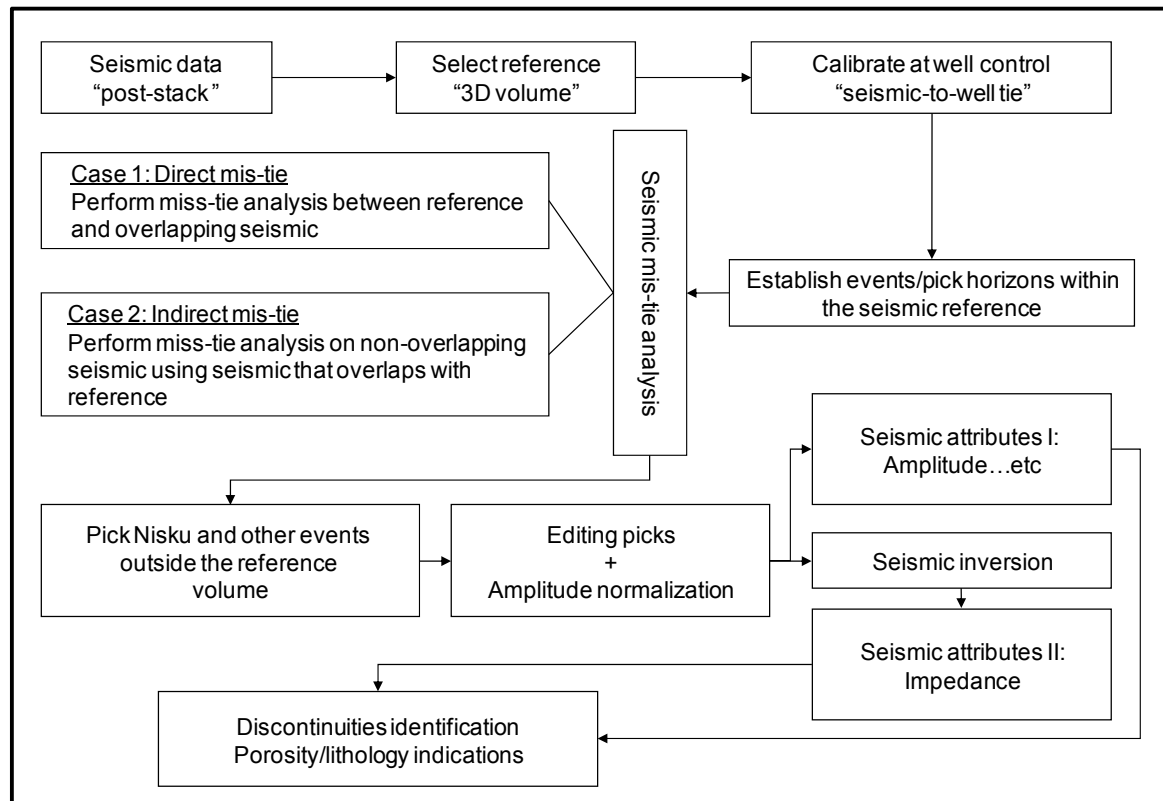


Figure 2: Flowchart outlining the major steps followed in the seismic data calibration and normalization.

Starting with the reference 3D volume, which is the largest brown rectangle in the middle of Figure 1, the majority of the seismic events were identified and picked. The seismic-to-well tie was made at various locations using available borehole data. Overall, the seismic data exhibit good ties to the synthetic seismograms, with the correlation coefficient ranging from 0.7 to 0.9. Figure 3 shows examples of the seismic-to-well tie near the water source well (1F1-11-29-45-2W5), at which a very good correlation is obtained (0.92).

Following the seismic-to-well tie and identification of seismic events within the reference 3D volume, data calibration was begun by first applying a time and phase shift and amplitude adjustments to those 2D seismic lines overlapping the reference 3D volume. The calibrated overlapping lines were then used to calibrate those that do not overlap the reference 3D volume. The process was repeated until all data were calibrated with respect to the reference 3D volume. Once the data were calibrated, their seismic amplitudes were normalized to a root-mean square (RMS) value of 1.0 using a time window designed to include the Nisku Formation.

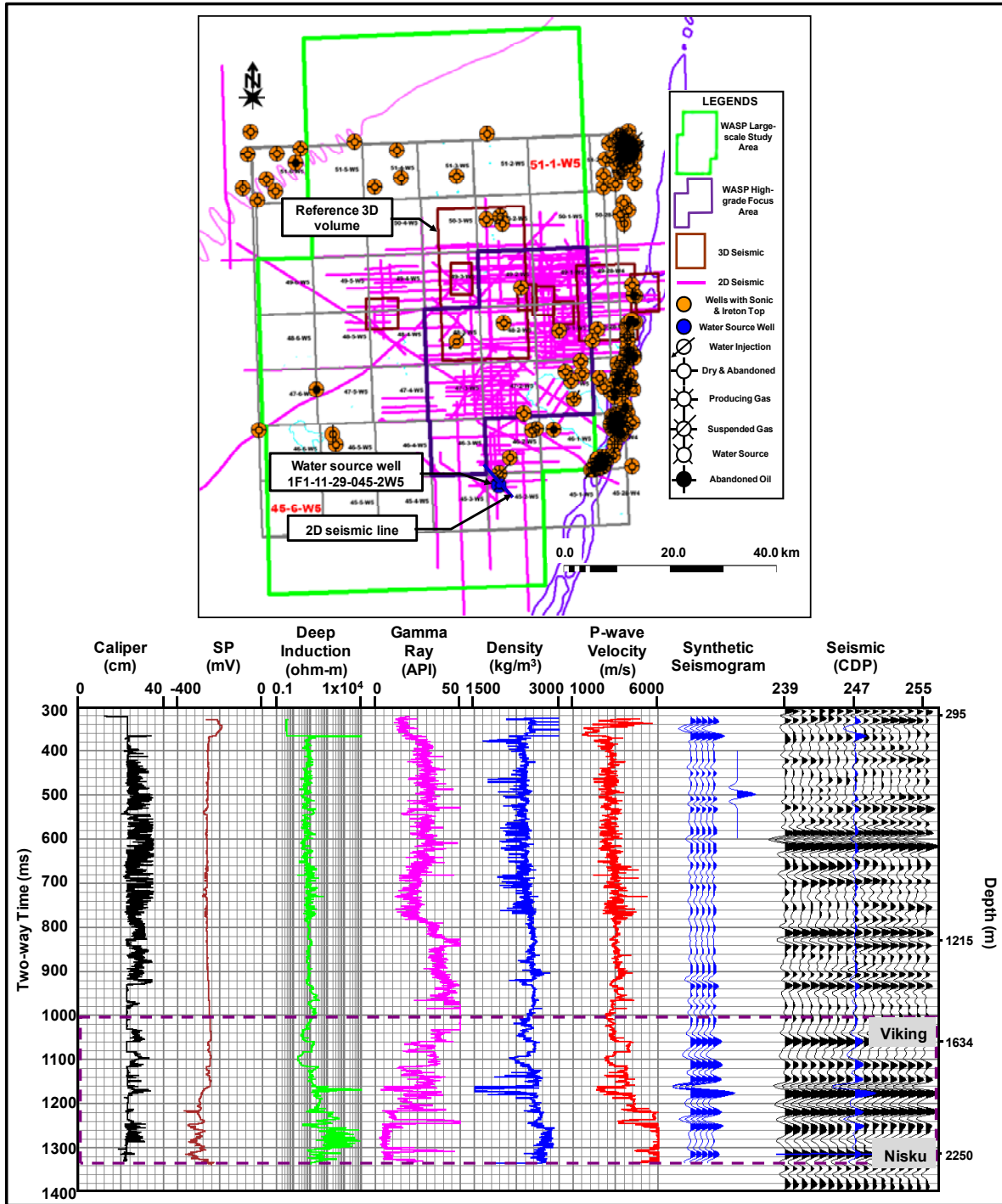


Figure 3: Seismic-to-well tie at the water source well (1F1-11-29-45-2W5). The location of the well and the seismic line (blue) are shown on the map. The correlation coefficient is 0.92 over the outlined zone (dashed rectangle) in the bottom image.

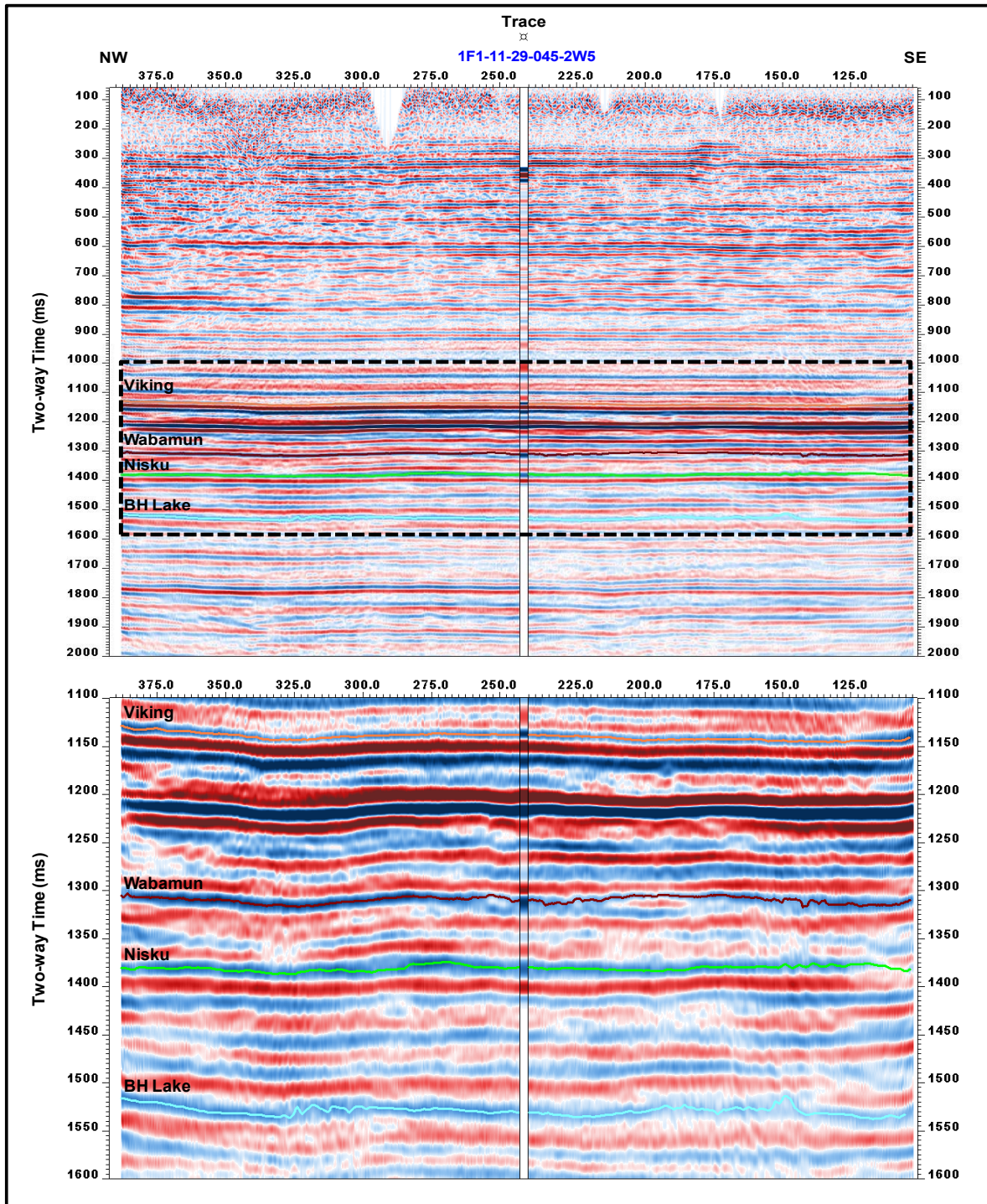


Figure 4: The 2D seismic line shown in Figure 3 with the synthetic track inserted at the well location (1F1-11-29-45-2W5). The seismic-to-well tie over the zone of interest enclosing the Nisku event (dashed rectangle) is enlarged in the bottom image.

3. REGIONAL TREND: 2D SEISMIC DATA

The regional seismic expression encountered in the study area is depicted in four of the regional LITHOPROBE 2D seismic lines (Figure 5 through 8). Several seismic events were identified throughout these regional lines, including: the Viking, the Wabamun, the Nisku, and the Beaverhill Lake events, as well as a Precambrian marker. The Viking Formation is composed of sandstone and is part of the Lower Cretaceous series. The Wabamun Formation, on the other hand, is mainly made of dolostone and it is the shallowest formation in the Upper Devonian strata that also includes the underlying dolomitized Nisku Formation. The reflection from the Beaverhill Lake Formation marks the transition between the Upper and Middle Devonian. The Precambrian marker represents the reflection from what it thought to be the Basal Sandstone Formation. In all the seismic lines the Nisku and underlying top Ireton events are represented by one period of the seismic data.

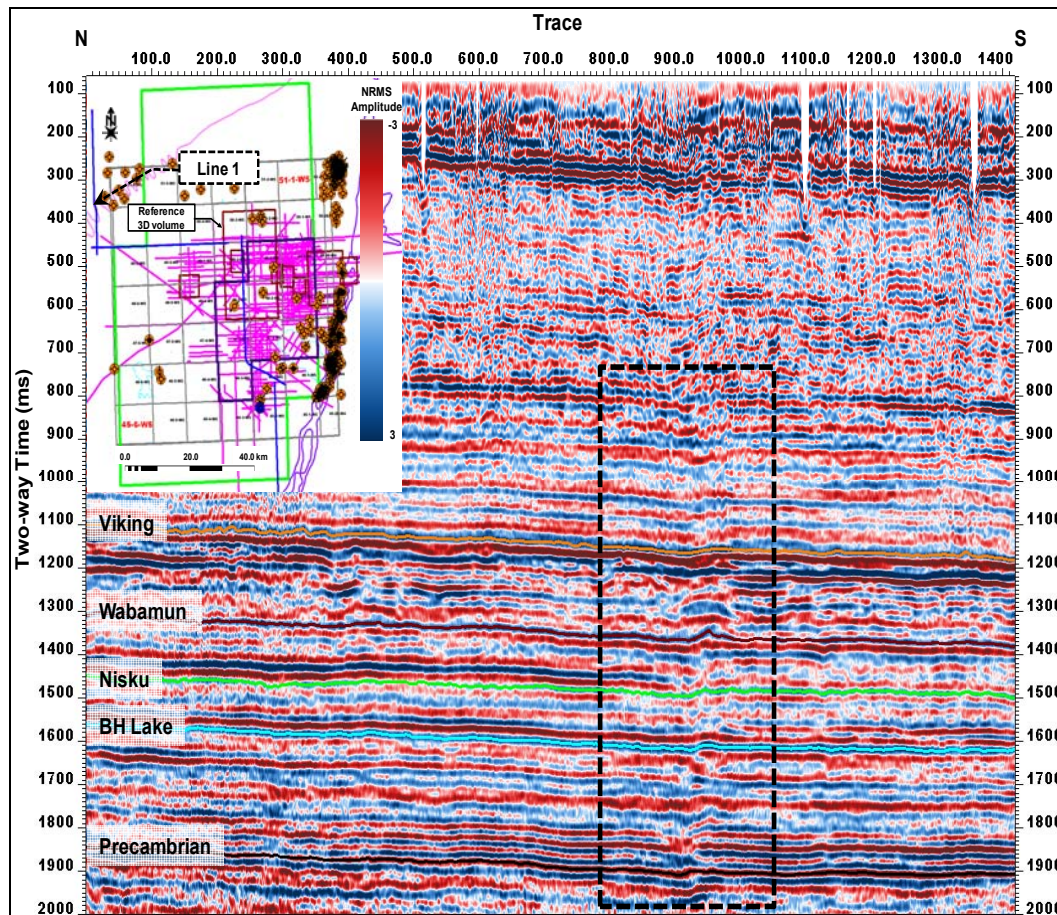


Figure 5: Line 1 of the LITHOPROBE regional 2D seismic data with some of the major seismic events identified, including the Nisku. The location of Line 1 is shown by the blue line in the inset base map. The dashed arrow in the inset base map points to the location of a sudden change in the time structure (dashed rectangle), which could be associated with the Moon Lake reef boundary or simply a result of Line 1 turning into the updip direction. BH Lake is the Beaverhill Lake event.

In Line 1 (Figure 5) there is a small change in the Nisku time structure as the line turns southward at trace 950 (within the dashed rectangle). This occurs near the Moon Lake reef boundary but it also coincides with a change in the survey orientation. A more interesting anomaly is outlined by the dashed rectangle in Line 2 (Figure 6), which marks the interpreted transition between the Nisku bank and the Nisku shale basin to the northwest. The regional dip, which is toward the southwest, is seen clearly on both Lines 1 and 2. In Line 3 (Figure 7), which traverses the WASP focus area in the north-south direction, the Nisku event is identified at approximately 1.37 s and is fairly flat. On Line 4 (Figure 8), the Nisku event is also flat and no major anomalous features can be identified in the Nisku. A sudden drop in the overlying Wabamun event is observed between traces 850 and 1100.

The variation in the Nisku event amplitude, as observed in these regional LITHOPROBE 2D sections, can be clearly seen in the NRMS amplitude map (Figure 11). The integrity of the Nisku Formation, as well as the integrity of the caprock (Calmar Formation), does not seem to be compromised in the focus area. Furthermore, none of the regional seismic lines exhibits any sign of major faulting. However, the dashed ellipse in Line 3 (Figure 7) indicates the location of a local discontinuity in the Wabamun event. This and similar anomalies are more clearly imaged by the 3D seismic data and will be discussed in the next section.

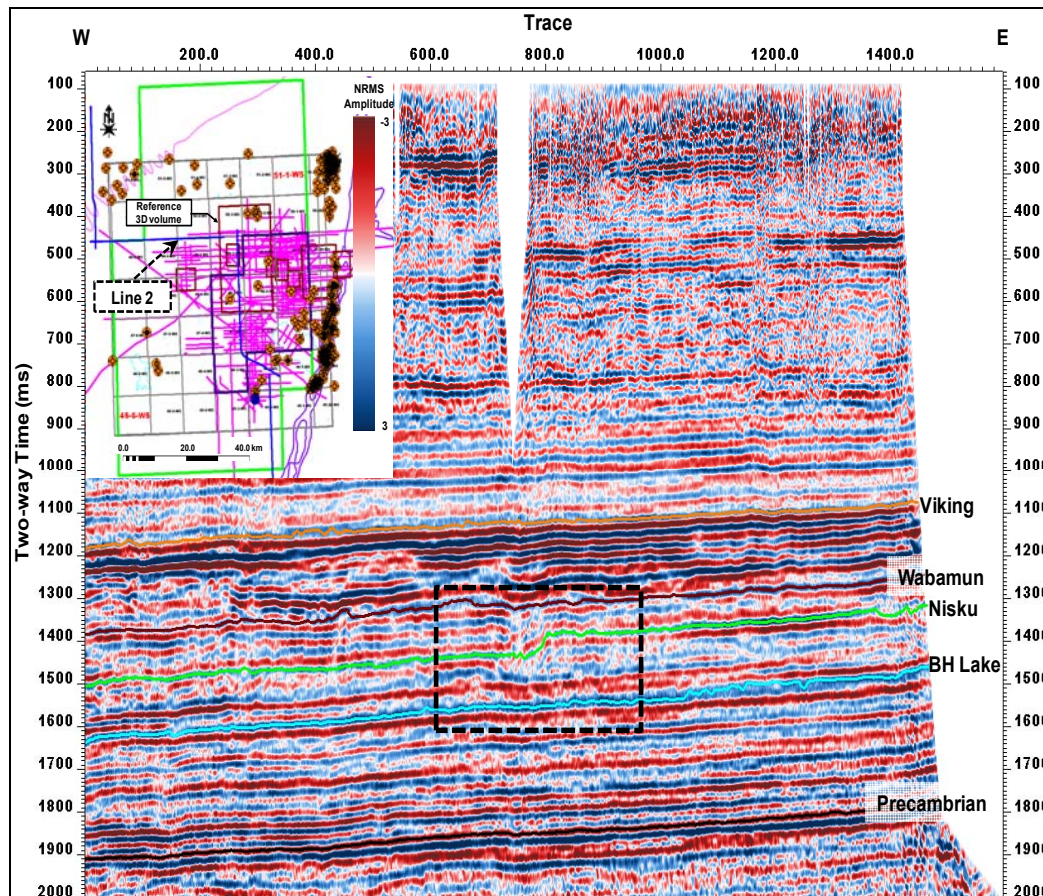


Figure 6: Line 2 of the LITHOPROBE regional 2D seismic data with some of the major seismic events, identified including the Nisku. The location of Line 2 is shown by the blue line in the inset base map. The dashed arrow in the inset base map points to the location of the transition between the Nisku bank and Nisku shale basin (dashed rectangle). BH Lake is the Beaverhill Lake event.

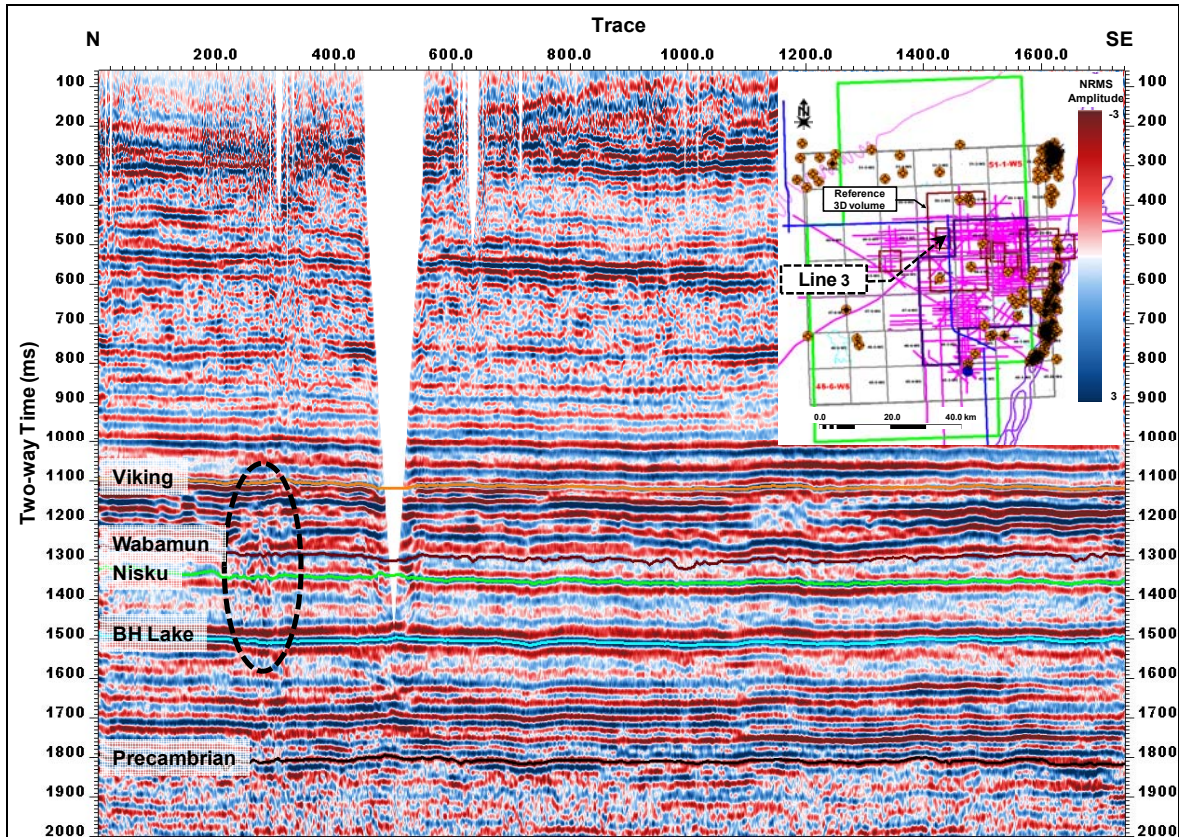


Figure 7: Line 3 of the LITHOPROBE regional 2D seismic data with some of the major seismic events identified, including the Nisku. The location of Line 3 is shown by the blue line in the inset base map. The dashed arrow in the inset base map points to the location of the dashed ellipse, which marks a local anomaly interpreted to be caused by a discontinuity in the Wabamun event. BH Lake is the Beaverhill Lake event.

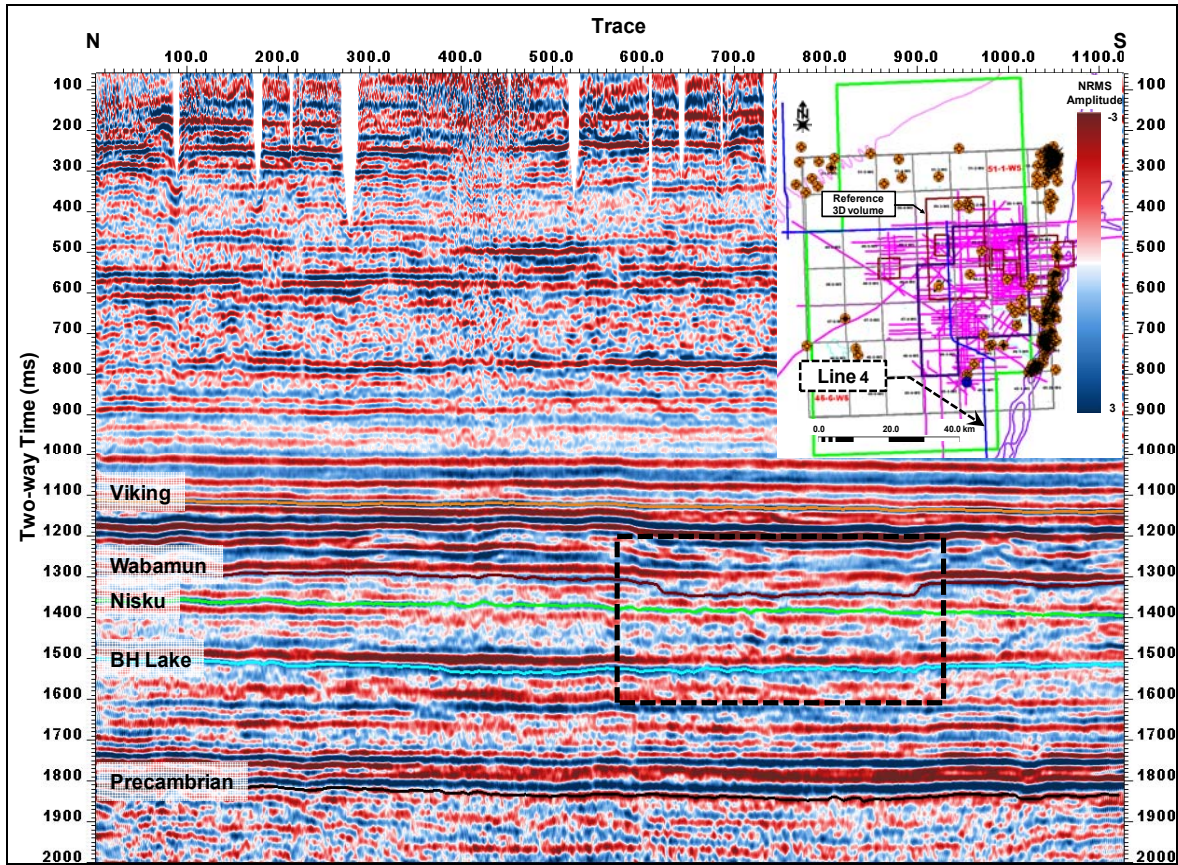


Figure 8: Line 4 of the LITHOPROBE regional 2D seismic data with some of the major seismic events identified, including the Nisku. The location of Line 4 is shown by the blue line in the inset base map. The dashed arrow in the inset base map points to the location of the dashed rectangle enclosing a local depression in the Wabamun event. BH Lake is the Beaverhill Lake event.

4. LOCAL TRENDS: 3D SEISMIC DATA

The interpretation of the Nisku Formation in the WASP focus area is fundamentally driven by the analysis of the time structure (Figure 9 and 10) and NRMS amplitude maps (Figure 11 and 12) from the 3D seismic data after calibration and amplitude normalization. In Figure 12 it is evident that only the amplitudes extracted from the 3D seismic data are reliable as the 2D seismic data are of poorer quality and do not exhibit a consistent areal pattern from which useful information could be extracted.

The time structure of the Nisku (Figure 10) is rather smooth and does not exhibit any significant variations within the WASP focus area expect for following the regional dip in the northeast-southwest direction. There are local lows, such as the one associated with the discontinuity and the depression in the Nisku time structure east of the reference 3D volume (Figure 10). However, the Nisku NRMS amplitude map (Figure 12) has proven more robust in identifying several anomalies in the area. Those include karsting (k) and discontinuities (d) originating in the Wabamun, as well as low (l) and high (h) amplitude anomalies and thinning (t) of the Nisku Formation itself.

In order to delineate those anomalies in Figure 10 and 12, an arbitrary multi-segment seismic line was extracted from the reference 3D volume (Figure 13). The first and most prominent anomaly is the karsting associated with dissolution in the overlying Wabamun Formation (k in Figure 14). The seismic data indicate that the karsting covers an area of approximately 7 km² north-northwest of the WASP focus area. Other anomalies are more localized, such as the discontinuities (d in Figure 14). The data indicate that they are also originating within the Wabamun Formation. The amplitude map reveals significant variations within the Nisku Formation lithology as indicated by the undulation from low to high amplitude as well as interpreted thinning, especially within the northern and eastern regions of the reference 3D volume (l, h and t in Figure 14). Table 2 summarizes the geological features interpreted from the multi-segment line (Figure 14). Some of the anomalies will be discussed again later in this report using additional seismic attributes.

As far as the Wabamun discontinuities are concerned, it is uncertain as to what they represent and what process might have caused them, but there are two suggested explanations: the first is a mechanical process while the second is a chemical process. The mechanical process suggests that these discontinuities are actually rhombochasm, a phenomena associated with strike-slip faults in which vertical fault surface bends in the fault plane direction. However the lack of spatial (Figure 12) and temporal continuity (Figure 14) does not seem to support this explanation, as the observed discontinuities tends to be isolated and exhibit circular generally patterns. The other explanation is that chemical processes, namely dissolution, such as those responsible for producing karsting, are responsible for those discontinuities. A dissolution agent, i.e., water, would travel along conduits, such as sub-seismic fractures, and thus dissolve parts of the Wabamun even at such a small scale. However, it is suggested that dissolution in the Wabamun should display a wider areal pattern, which is not the case with these discontinuities. In any case, it is believed that those discontinuities may pose a risk and, therefore, should be taken into consideration for the location of a future CO₂ injection program.

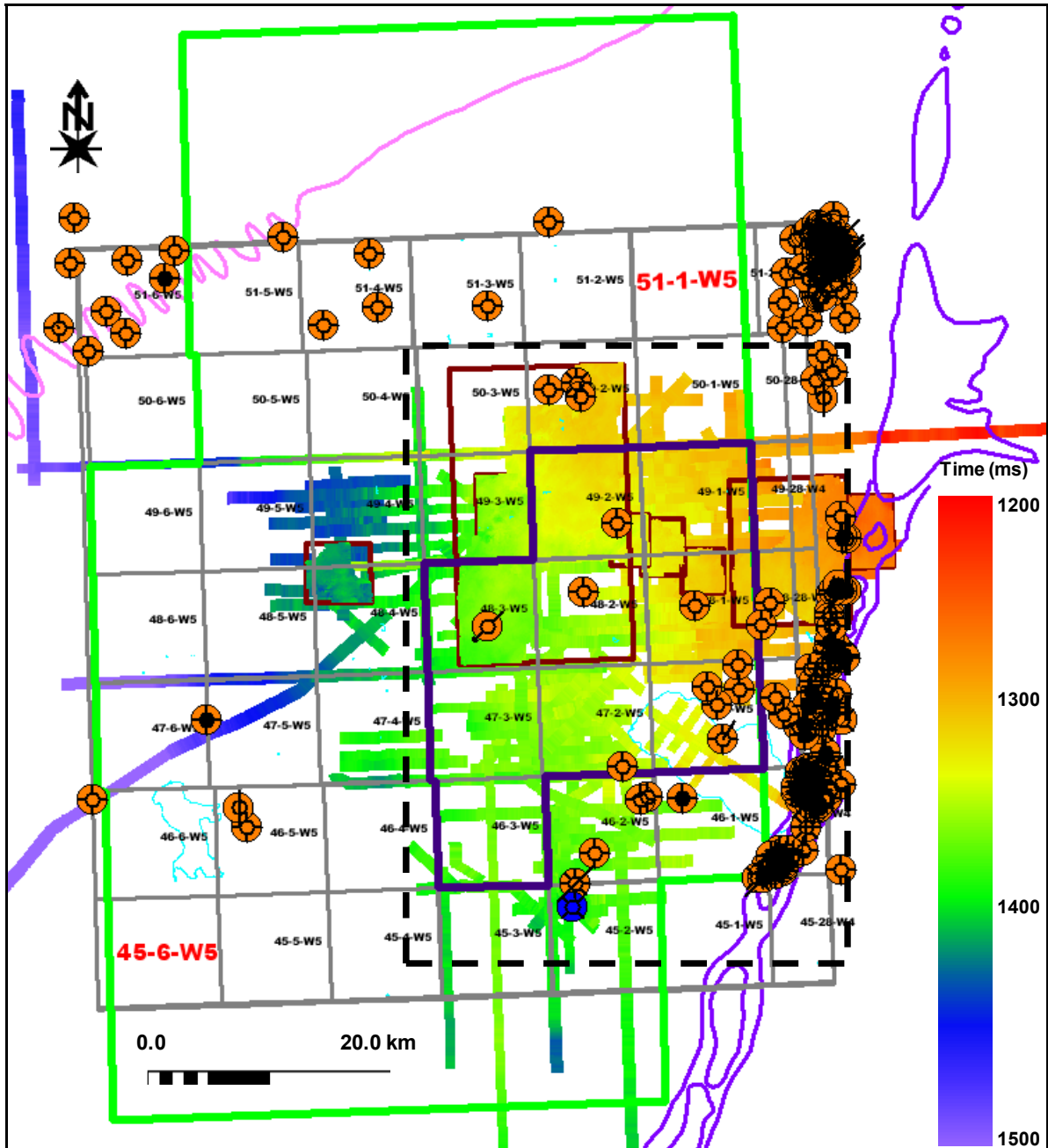


Figure 9: The time structure of the Nisku event after data calibration. The dashed black rectangle shows the extent of the zoom-in display over the study area in Figure 10.

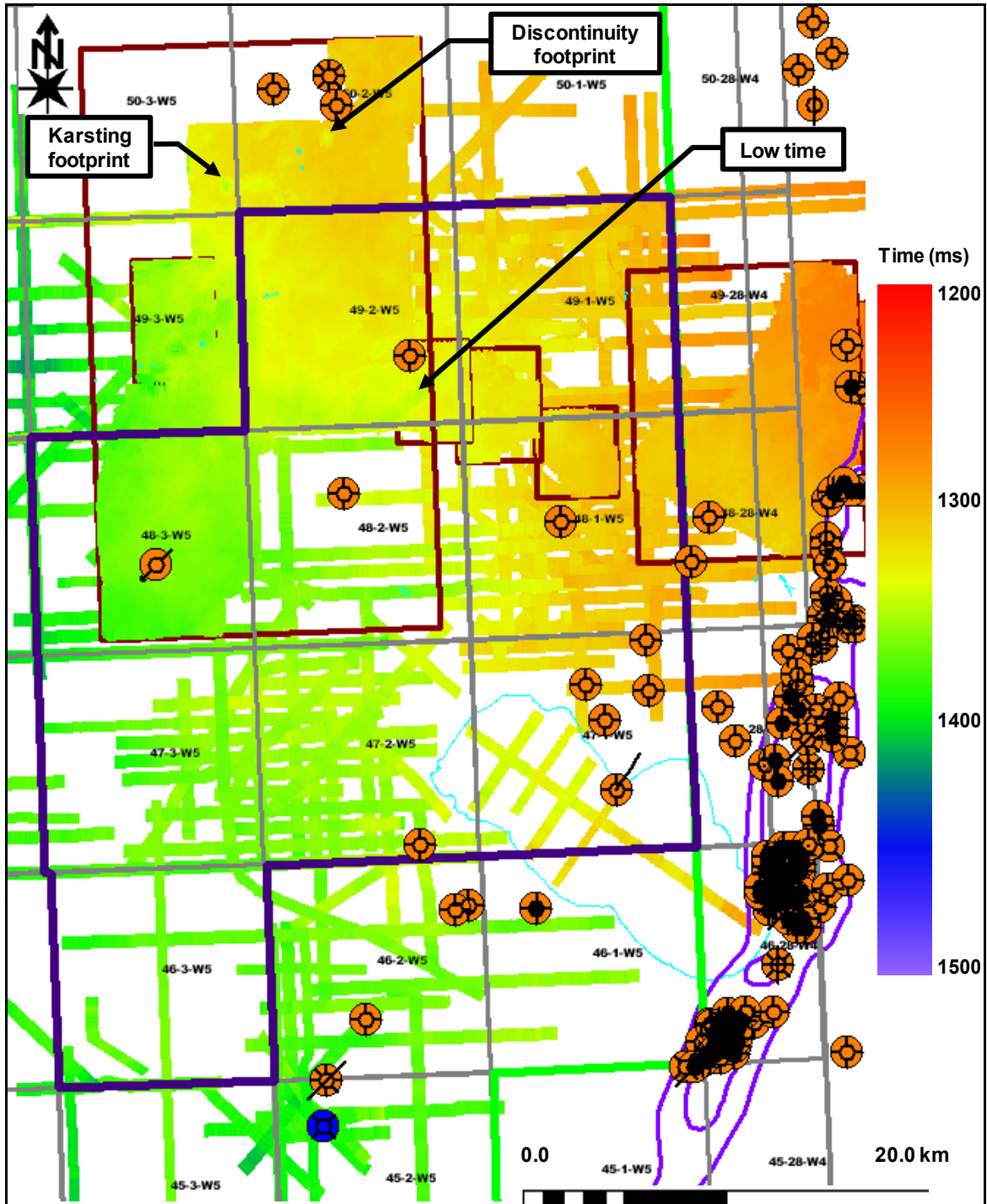


Figure 10: Zoom-in display of the Nisku time structure map in Figure 9. The locations of some of the major anomalies are specified: Wabamun karsting (see Figure 14), Wabamun discontinuities, and the Nisku local time low. It should be emphasized that the karsting and discontinuity effects shown here are the footprints of those anomalies and do not indicate that the Nisku has been physically affected.

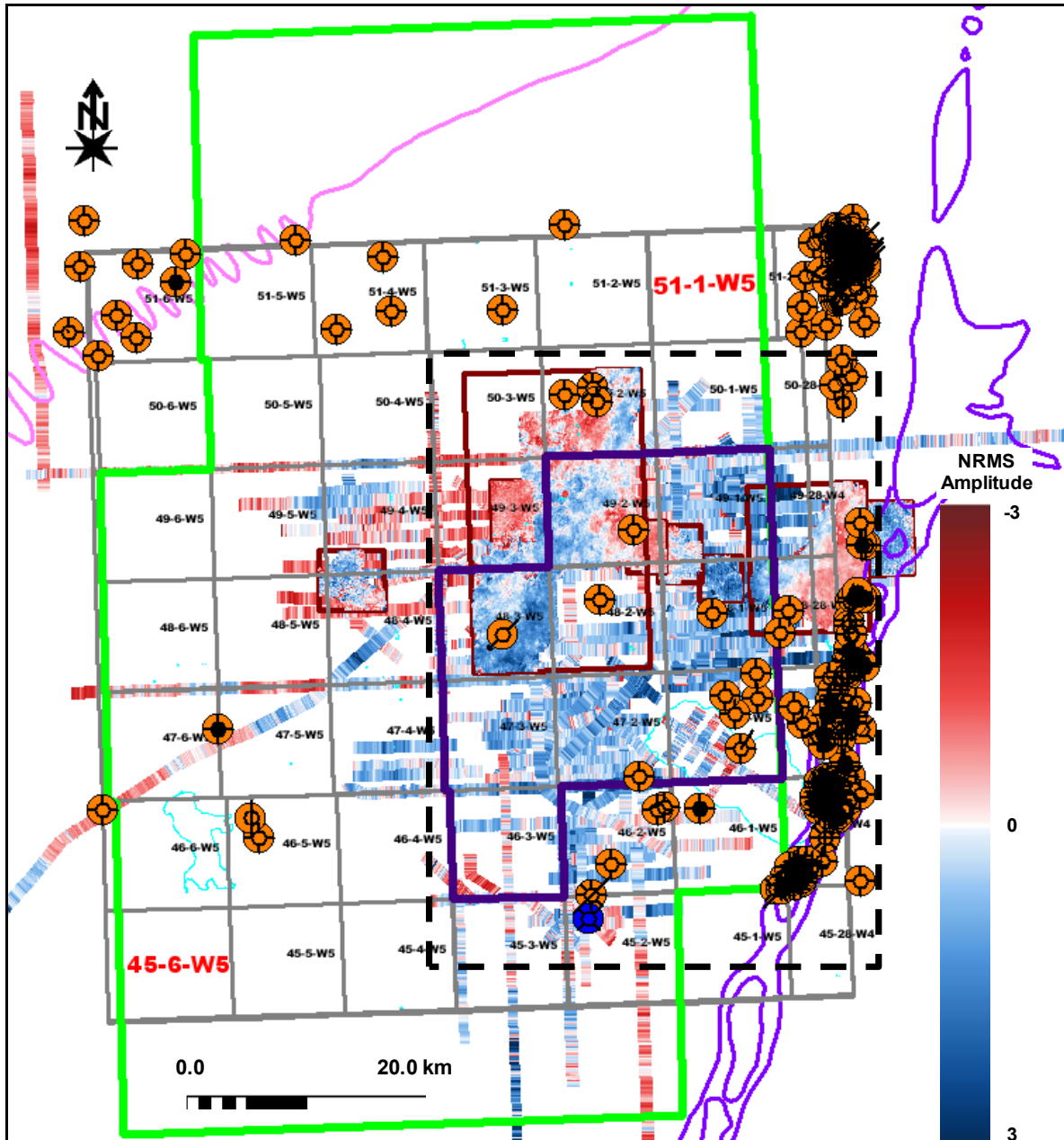


Figure 11: NRMS amplitude map of the Nisku event after data calibration and RMS amplitude normalization. Note the strong variations in the Nisku amplitude map compared to the time structure map. The dashed black rectangle shows the extent of the zoom-in display over the study area in Figure 12.

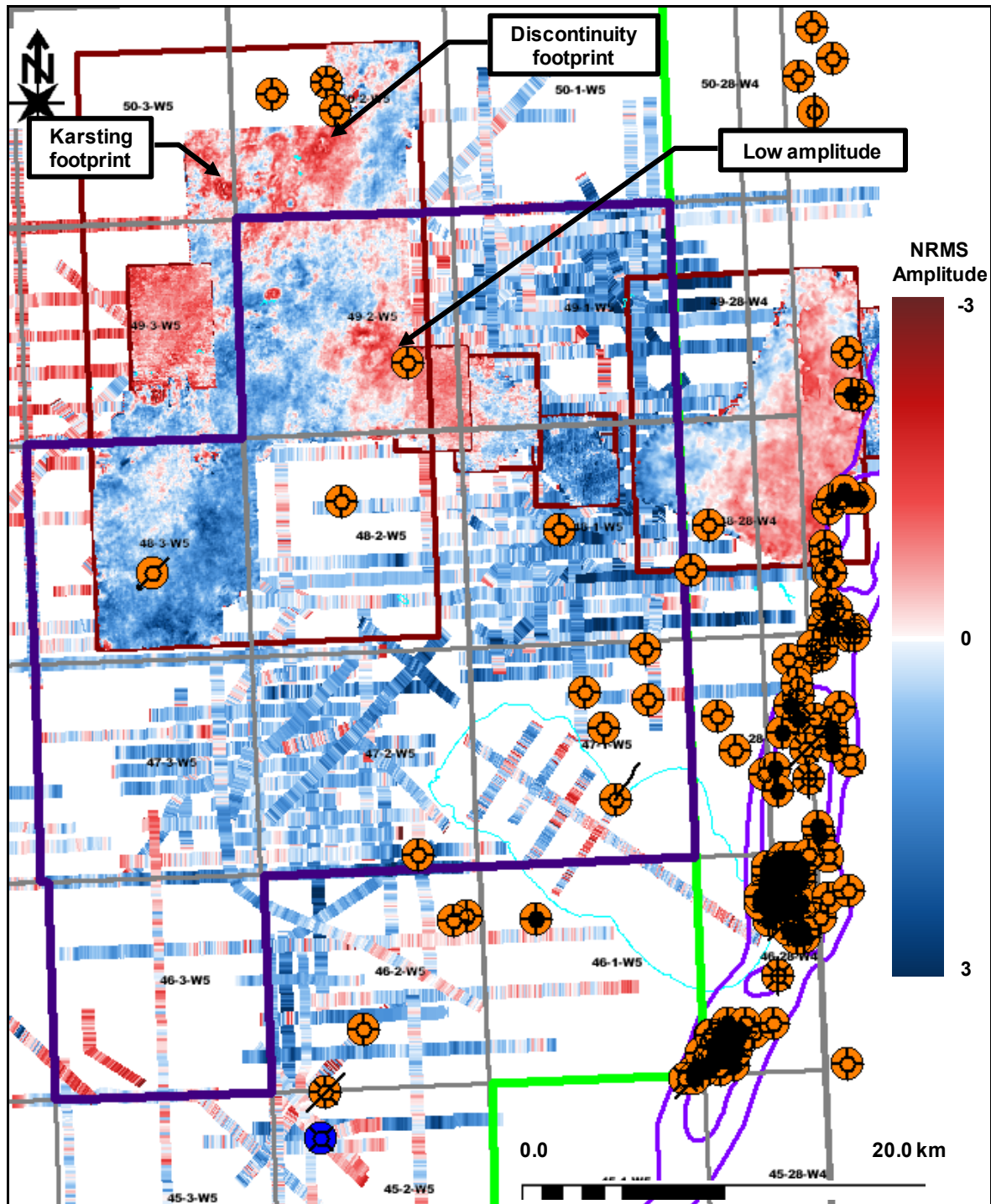


Figure 12: Zoom-in display of the Nisku NRMS amplitude map in Figure 11. Some of the major amplitude anomalies are specified: Wabamun karsting (see Figure 14), Wabamun discontinuities, and the Nisku amplitude low. It should be emphasized that the karsting and discontinuity effects shown here are the footprints of those anomalies and do not indicate that the Nisku has been physically affected.

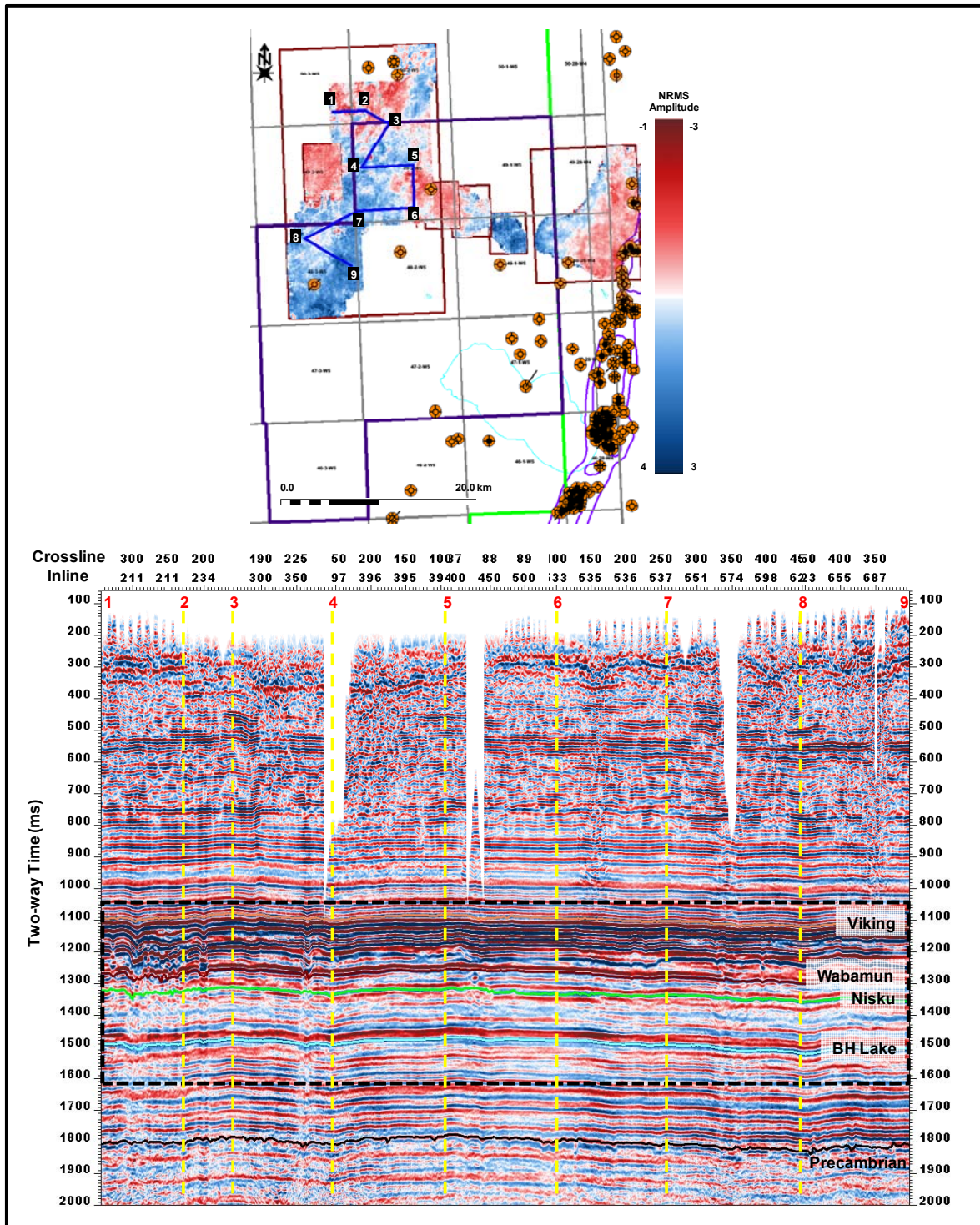


Figure 13: A multi-segment seismic section passing through some of the geological features within the reference 3D volume. The base map shows the location and orientation of the multi-segment section. The nodes are shown at their corresponding location along the horizontal axis. The right side of the colour scale in the base map represents the amplitude within the section (-3 to 3). The dashed rectangle indicates the extent of the zoom-in display in Figure 14.

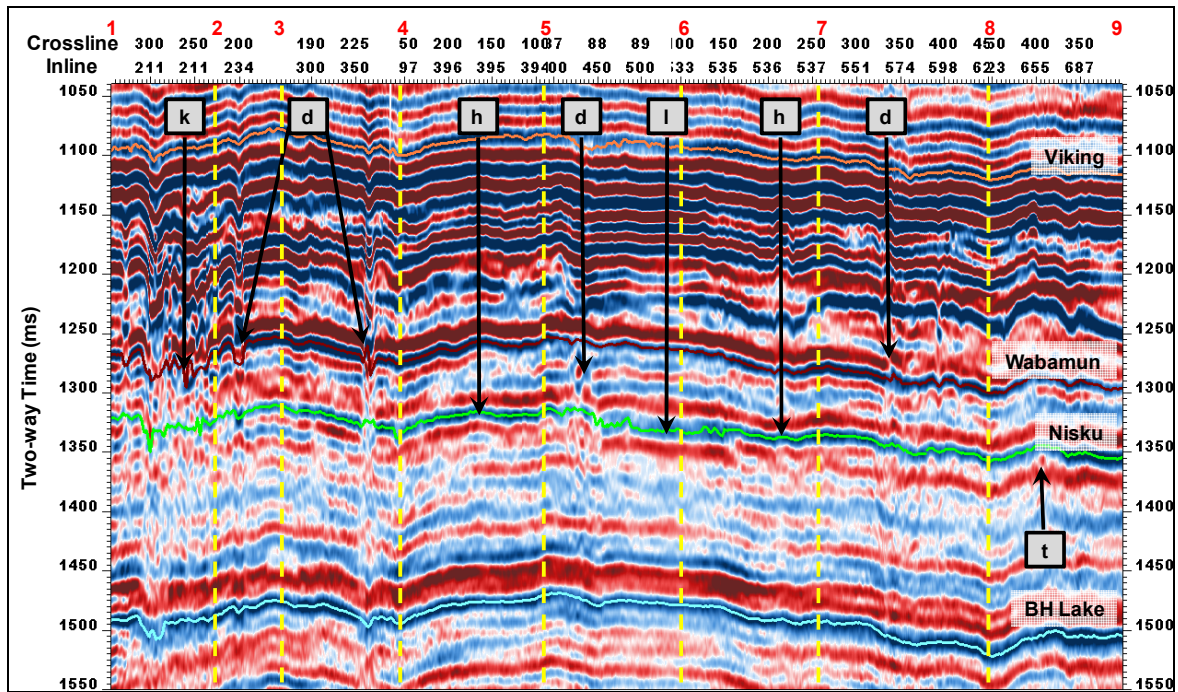


Figure 14: A zoom-in display of the multi-segment line through the 3D volume in Figure 13. Segment 1-2 passes through the karsting (k) originating in the Wabamun event. Segments 2-3 and 3-4 cross local Wabamun discontinuities (d). Segments 4-5, 5-6, and 6-7 show an example of the Nisku amplitude changing from high (h) to low (l) to high (h) again. Note the broadening in the Nisku cycle in segment 5-6. Segment 7-8 shows some amplitude anomalies between 1150 and 1200 ms, which are interpreted to be associated with the Cretaceous strata. The change from moderate (m) to high (h) Nisku amplitude is illustrated in segment 8-9. Segment 8-9 also traverses an area of local Nisku amplitude thinning (t), which is mapped by the seismic attribute amplitude thickness of the peak (ATP).

Table 2: Summary of some of the geological features within the multi-segment line (Figure 14).

Segment	Feature	Description
1-2	k: karsting	Dissolution associated feature in the Wabamun event
2-3	d: discontinuity	Local amplitude anomaly within the Wabamun event
3-4	d: discontinuity	Local amplitude anomaly within the Wabamun event
4-5	h: high amplitude	High amplitude within the Nisku event
5-6	d: discontinuity	Local amplitude anomaly within the Wabamun event
	l: low amplitude	Low amplitude within the Nisku event
6-7	h: high amplitude	High amplitude within the Nisku event
7-8	d: discontinuity	Local amplitude anomaly within the Wabamun event
8-9	t: amplitude thinning	Decreasing duration of the Nisku event

5. INTERPOLATION AND DEPTH CONVERSION

In order to undertake depth conversion and produce a continuous depth structure map, the time structure map was interpolated using a kriging algorithm (a linear least-squares interpolation method) with a grid size of 50×50 m. Both 2D and 3D Nisku horizons were used in the interpolation and the result is shown in Figure 15. Following the time structure interpolation, a simple time-to-depth conversion was executed to generate the depth structure map (Figure 16). The conversion algorithm utilized the Nisku time structure (from the horizon picks) and the Nisku depths from borehole data within the study area.

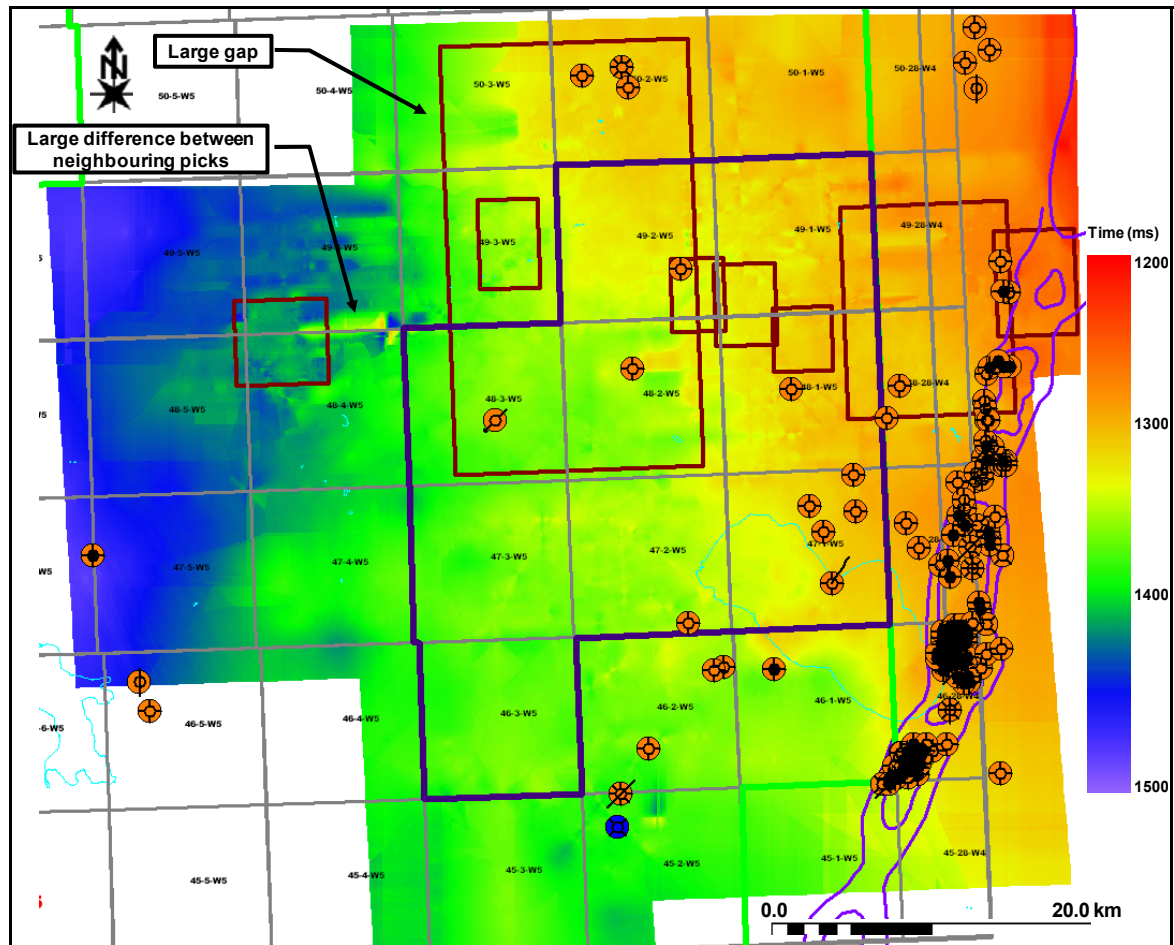


Figure 15: Interpolated time structure map (Figure 9) using a kriging algorithm with a grid size of 50×50 m.

In general, the interpolated time and depth structure maps (Figure 15 and Figure 16) honour the well data, as illustrated in Table 3, in which the well depths and the depth values estimated from the depth map are compared. However, the interpolation seems to produce inaccurate results in areas where there is a large gap in data coverage or where there is a relatively large difference between neighbouring picks (Figure 15). An additional cause of inaccuracy in the interpolated depth structure map is the absence of Nisku Formation picked depths in some of the borehole data (Figure 16). However, despite the few inaccuracies, the results suggest that the kriging interpolation algorithm has performed well within the WASP focus area. In addition to providing a more continuous perspective of the Nisku event, the interpolated time (Figure 15) and depth (Figure 16)

structure maps give an insight into the subtle depth variations in the Nisku Formation within the WASP focus area.

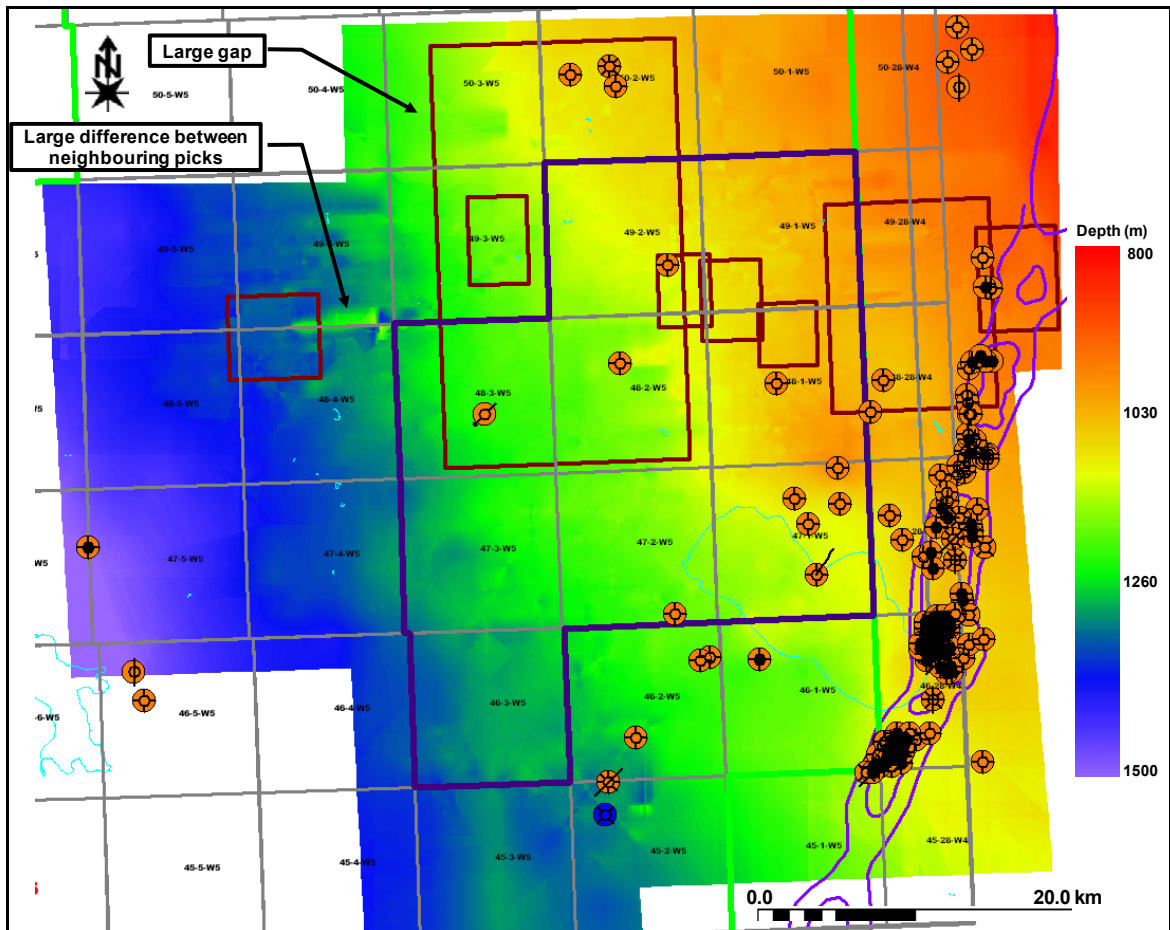


Figure 16: Interpolated depth structure map using a kriging algorithm with a grid size of 50×50 m.

Table 3: Comparison between the measured and estimated depth values using kriging algorithm (Figure 16). The difference between the two is also shown. The interpolation algorithm seems to honour the actual data, except at well 100163504701W500.

Well	Measured Depth (m)	Estimated Depth (m)	Difference (m)
100010104601W500	1111.6	1111.6	0.0
100020104601W500	1114.9	1114.9	0.0
100022104801W500	1178.6	1178.6	0.0
100022304828W400	1038.1	1038.1	0.0
100022804802W500	1148.1	1148.1	0.0
100022804802W500	1148.1	1148.1	0.0
100052005002W500	1075.1	1075.1	0.0
100060204702W500	1198.8	1198.8	0.0
100060204702W500	1198.8	1198.8	0.0
100061504803W500	1219.5	1219.5	0.0
100062904601W500	1170.6	1170.6	0.0
100082604701W500	1082	1082.7	-0.7
100090104601W500	1104.8	1106.4	-1.6
100091004701W500	1107.9	1101.1	6.8
100092404706W500	1488	1488	0.0
100100904602W500	1257.9	1257.9	0.0
100102105002W500	1063.3	1063.3	0.0
100102204701W500	1098.2	1098.2	0.0
100102504602W500	1200	1200	0.0
100122704701W500	1098.8	1099	-0.2
100131104828W400	1042	1042.4	-0.4
100131304728W400	1066.8	1066.8	0.0
100142904605W500	1502.2	1502.2	0.0
100143204502W500	1285.3	1285.3	0.0
100151104902W500	1092.1	1093	-0.9
100152304728W400	1069.8	1069.8	0.0
100161605002W500	1063.5001	1062.9	0.6
100163504701W500	1292.1	957.9	334.2
102122504602W500	1197.9	1197.9	0.0
1F1112904502W500	1297	1297	0.0

6. NUMERICAL MODELLING

Seismic amplitude plays an important role in seismic interpretation and site characterization. In this project, substantial emphasis has been placed on the Nisku event amplitude to provide one approach for favourable injection site selection. In general, the seismic amplitude response can be modelled as a function of the following parameters:

$$\text{Seismic Amplitude} \propto f(\text{thickness}) + f(\text{impedance}) + f(\text{wavelet}) + \text{noise} \quad 1$$

Where $f(\text{thickness})$ represents the change in the Nisku thickness, $f(\text{impedance})$ represents the change in its acoustic impedance (P-wave velocity multiplied by the density), $f(\text{wavelet})$ is the seismic wavelet, and noise is the amount of noise present in the data. Prior to undertaking the modelling, it was important to decide on the range of these parameters and their effect on the seismic amplitude. Therefore, taking into consideration the data calibration and normalization in addition to examining the well control in the study area, we observed the following:

1. The Nisku Formation thickness in the study area varies between 40 and 80 m and thus thickness should be taking into consideration as a primary element in the modelling.
2. The Nisku Formation acoustic impedance (I_p) is another critical parameter that has to be included in the modelling. However, by examining the well control, it was found that the Nisku impedance is mainly driven by variations in P-wave velocity rather than density:

$$\Delta I_p = \Delta \alpha \times \Delta \rho \approx \Delta \alpha \quad 2$$

Where α is the P-wave velocity in m/s and ρ is the density in kg/m^3 . The average P-wave velocity ($\alpha_{\text{avg.}}$) of the Nisku Formation was found to vary between 5500 m/s and 6500 m/s.

3. The wavelet is assumed to be stationary; this follows from the data calibration.
4. The noise is assumed to be random; therefore adding it contributes insignificantly to the observed amplitude.

Based on these observations and after running some sensitivity analyses, it was decided that thickness and average P-wave velocity are the primary Nisku parameters affecting the seismic Nisku event amplitude. Subsequently, zero-offset synthetic seismograms were generated using a 25 Hz Ricker wavelet and the convolutional model to further understand the effect of these two parameters on the Nisku event's amplitude and time, and effect on the underlying Ireton event. Figure 17 is a side-by-side panel display illustrating the thickness and average P-wave velocity effect on time and amplitude of the Nisku and Ireton events. In order to better discern the individual effects, the time and amplitude associated with those two events were picked using the peak at approximately 1130 ms for the Nisku event and the underlying trough (~ 1170 ms) for the Ireton event.

For the Nisku event, the modelling results (Figure 18 and 19) suggest that the amplitude variations in the study area, excluding those associated with discontinuities footprint, are most likely due to variability in the average acoustic impedance (mainly average P-wave velocity) rather than thickness. For instance, changing the average velocity (vertical axis) will cause over a 60% change in amplitude whereas changing the thickness (horizontal axis) will only cause about an 8% variation in amplitude (Figure 19). The highest amplitude effect is observed for a high average P-wave velocity. The results also suggest that there would be a time shift in the Nisku event, and it would be more prominent at relatively low Nisku thickness values and an average P-wave velocity. Figure 20 illustrates the footprint effect on the Ireton event as a result of changing the thickness and

average P-wave velocity of the Nisku Formation. As expected, the maximum time delay in the Ireton event time is associated with low average Nisku P-wave velocity whereas the highest amplitude change correlates with high average Nisku P-wave velocity. In all the modelling results (Figure 18 and 20), the conclusion is that the highest sensitivity in the seismic amplitude and travel time is associated with changes in the average P-wave velocity rather than thickness.

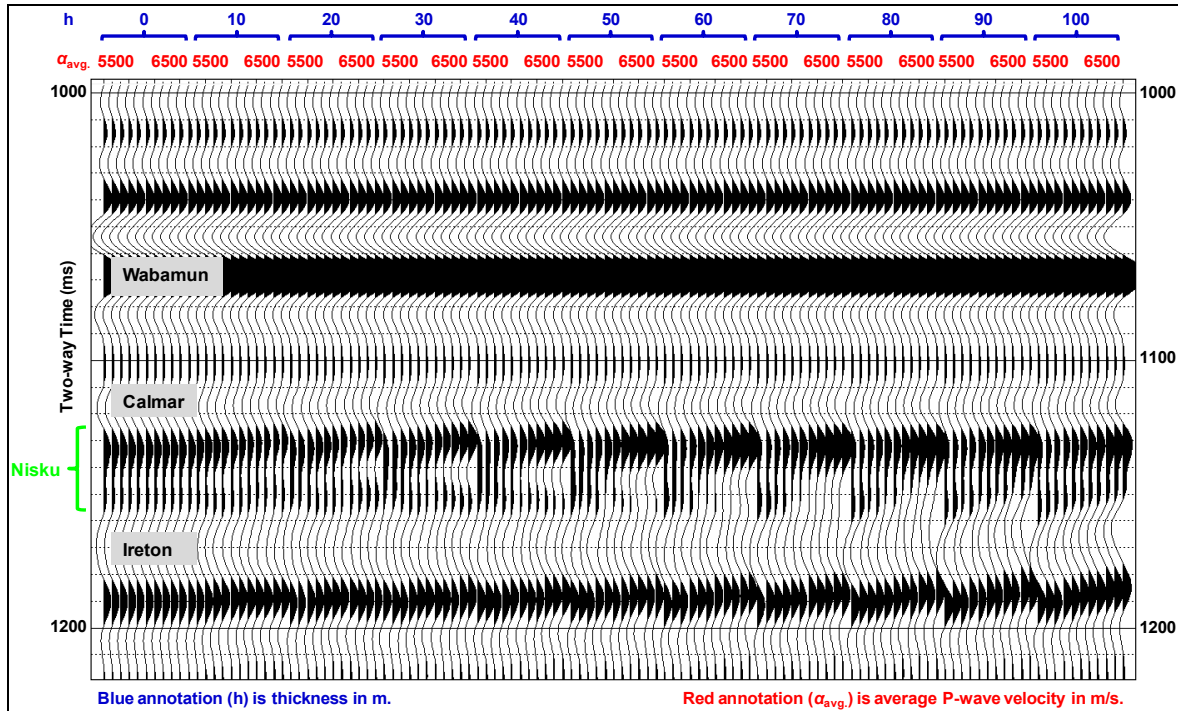


Figure 17: Sequential display of the normal incidence synthetic seismogram in which the Nisku event amplitude is modelled as function of thickness and average P-wave velocity. The top of the Nisku event is identified as the peak at approximately 1130 ms (the green bracket along the time axis approximates the frequency cycle through the formation). In each blue bracket (thickness effect), there are 11 traces, each representing the seismic amplitude associated with that thickness and an average Nisku P-wave velocity increasing from 5500 m/s to 6500 m/s at an increment of 100 m/s. The modelling was undertaken using well 100-10-05-052-02W5. The actual Nisku thickness and average P-wave velocity at this well are 100 m and 6100 m/s, respectively.

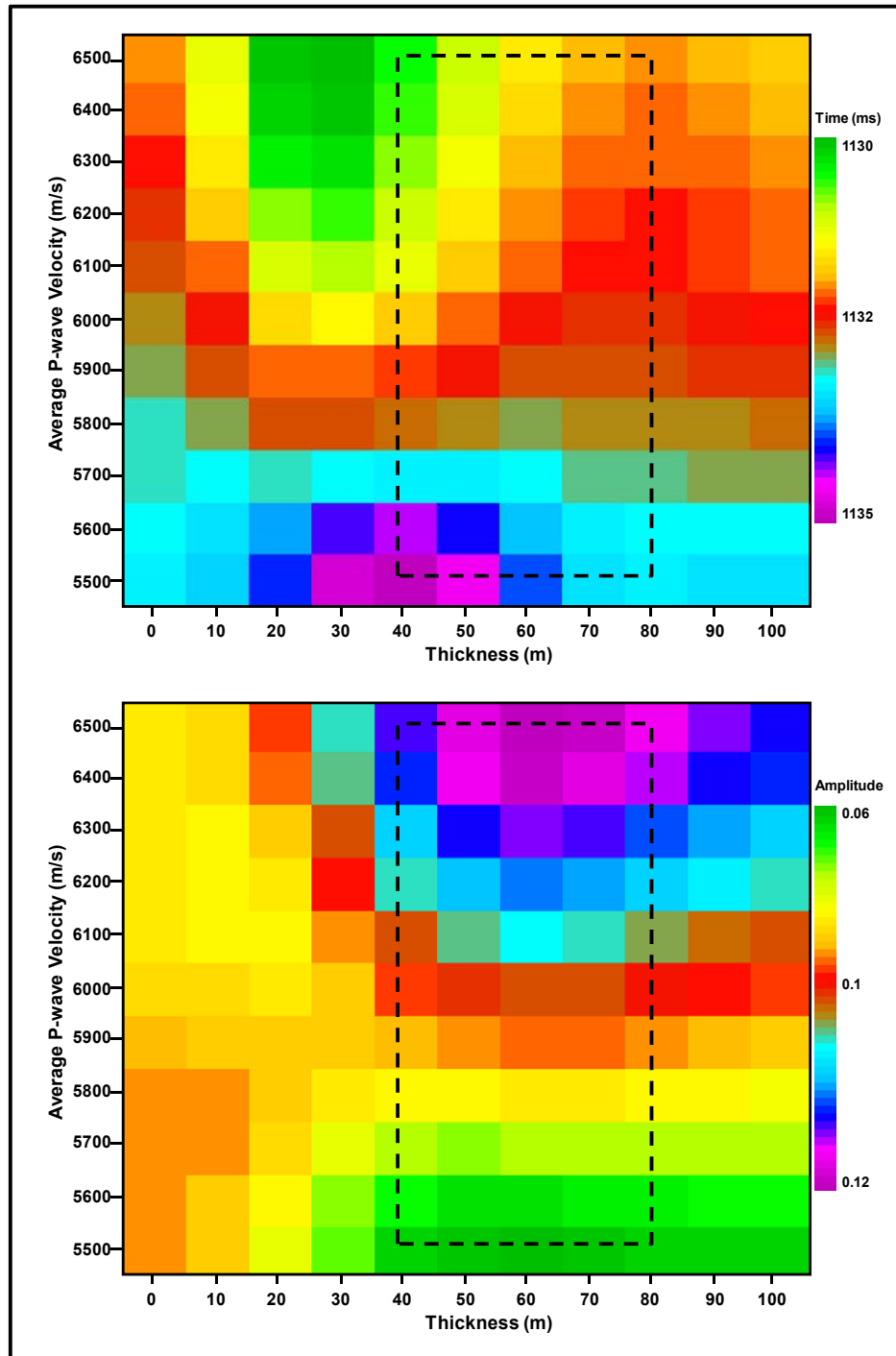


Figure 18: Nisku event amplitude (top) and time (bottom) as a function of thickness and average P-wave velocity. The actual Nisku thickness and average P-wave velocity are 100 m and 6100 m/s, respectively. The maps represent the Nisku amplitude and time horizons that resulted from picking the peak amplitude corresponding to the Nisku event in Figure 17. The black dashed rectangle outlines the most likely Nisku thickness and average velocity values within the study area based on well control. The results suggest that the Nisku average P-wave velocity (or impedance) effect is far more significant than the thickness effect. Thus, the highest sensitivity is along the vertical axis.

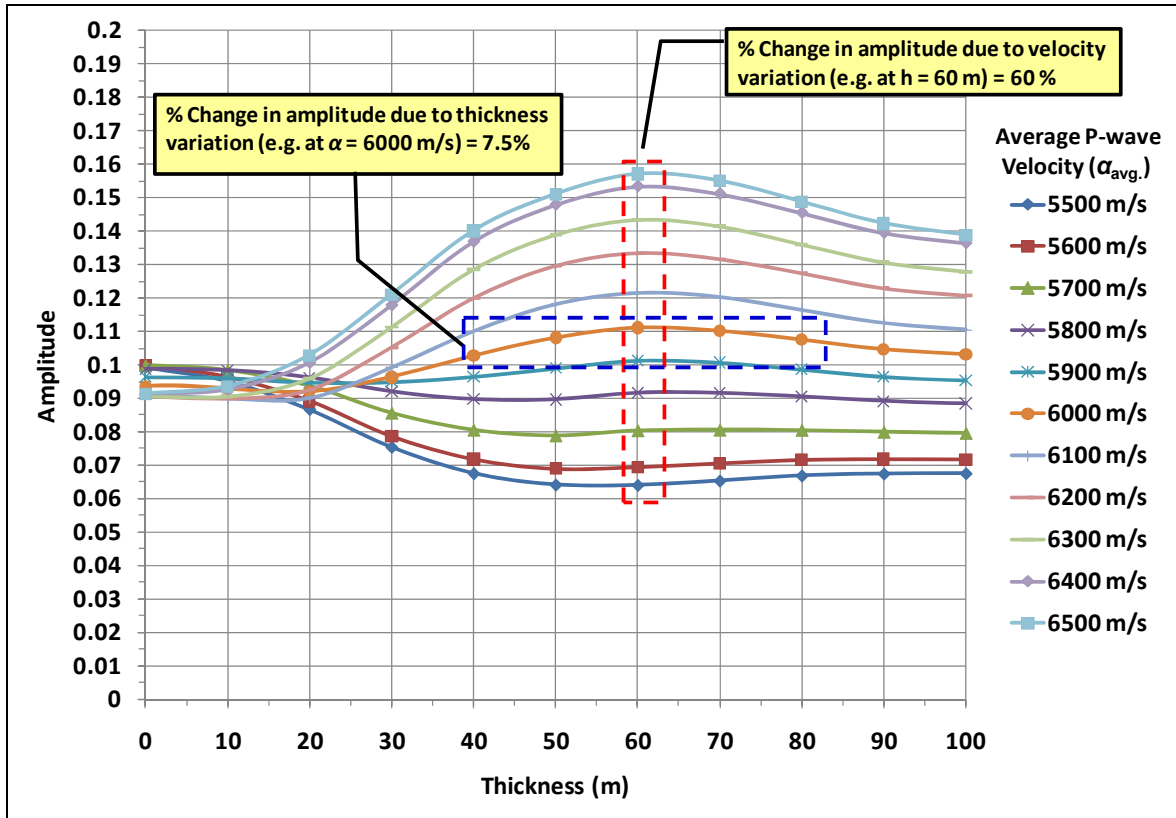


Figure 19: Nisku amplitude modelling result in which the difference between the thickness and average P-wave velocity effect on the Nisku event amplitude is evident. The actual Nisku thickness and average P-wave velocity are 100 m and 6100 m/s, respectively.

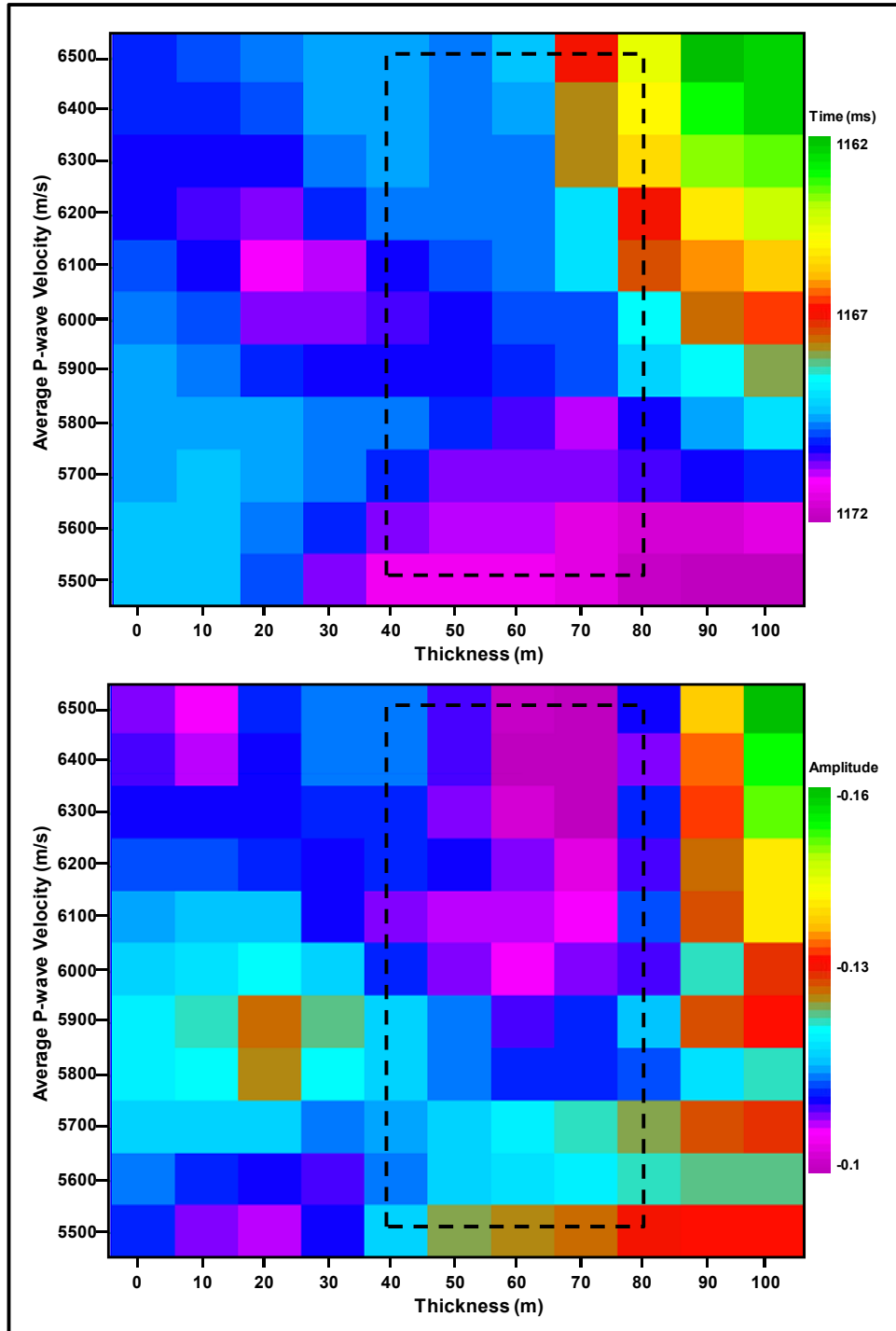


Figure 20: Ireton event amplitude (top) and time (bottom) as a function of Nisku thickness and average P-wave velocity. The maps represent the Ireton amplitude and time horizons that resulted from picking the trough amplitude corresponding to the Ireton event in Figure 17. The black dashed rectangle outlines the most likely Nisku thickness and average P-wave velocity values within the study area based on well control. The results suggest that the effect of the Nisku average P-wave velocity (or impedance) footprint on the Ireton event is far more significant than the thickness effect.

7. SEISMIC ATTRIBUTES

In addition to amplitude, several seismic attributes, such as the average NRMS amplitude (Figure 21), the amplitude thickness of the peak (ATP) of the Nisku reflection (Figure 22) and difference attributes (Figure 24 and 25), were generated to strengthen the interpretation of the lithology changes and geologic discontinuities in the study area. Unlike acoustic impedance inversion (next section), those attributes are computed directly from the Nisku time and/or amplitude. For those attributes, only 3D seismic data were exploited as such attributes require, in addition to time and amplitude, continuous and dense two-dimensional spatial sampling, both of which are absent in the 2D seismic data.

The average NRMS amplitude of the Nisku event (Figure 21) was calculated over a window of 10 ms (centred on the Nisku horizon pick). The purpose behind this averaging is to generate another representation of the Nisku event amplitude that captures the amplitude envelope around the event rather than a single value and thus minimizes errors due to picking ambiguities. The computed average NRMS amplitude map is quite similar to the original NRMS amplitude map in Figure 12, which is an indication that the representation of the amplitude variations within the Nisku Formation in Figure 11 and 12 are appropriate. The only difference is that a new pattern emerges from the average NRMS amplitude map, as indicated in Figure 21. This pattern is better captured by the attribute called amplitude thickness of the peak (ATP).

The ATP (Figure 22) calculates the duration of the Nisku peak from zero-crossing to zero-crossing in ms; the peak being defined as amplitude value larger than zero value. One of the most interesting features associated with ATP is that it accounts very well for the transition between the various seismic volumes, something that was not fully achieved with conventional amplitude maps (Figure 12 and 21). The low ATP values indicate areas where the Nisku amplitude peak thins. Such zones can also be seen in the seismic sections as indicated by the symbol “t” in the multi-segment line in Figure 14. The thinning appears to be mainly occurring at the base of the Nisku event and there are two explanations proposed for its cause. The first is that there might be an abrupt change in the thickness of the Nisku Formation. The second is that the thinning might be associated with a change in P-wave velocity resulting from either a facies change (shale content) or porosity variations within the Nisku Formation. In order to refine our interpretation, the ATP was calculated (Figure 23) using the synthetic seismogram in Figure 17. The ATP attribute is rather complicated and suffers from non-uniqueness, as depicted in Figure 23, in which two different formation thicknesses, at $\alpha_{avg} = 6500$ m/s for instance, yield the same ATP value. Unfortunately, there is insufficient well penetration through the Nisku Formation that could be used to better calibrate this attribute. Nonetheless, it is possible to reduce the non-uniqueness by integrating high ATP values with optimum values of other attributes (e.g., low impedance and high porosity), which are used as indicators for favourable site conditions in the study area.

The difference method is a member of another class of attributes, which, in contrast, is sensitive to discontinuities in seismic signal. The method is based on a simple algorithm that subtracts a given seismic trace from its neighbouring trace and divides by their sum (Luo et al., 1996). The method has proven robust in detecting various types of discontinuities encountered in the seismic data, as can be seen in Figure 24 and 25. To account for preferential direction, the difference attribute was computed in both the inline direction (Figure 24) and in the crossline (Figure 25) direction. The former was more robust in identifying geologic discontinuities within the reference 3D, such as the Wabamun karsting footprint on the Nisku event. The crossline difference, on the other hand, was more sensitive to variations associated with some of the other seismic volumes, for instance the local time low just east of the reference volume, as shown in Figure 10.

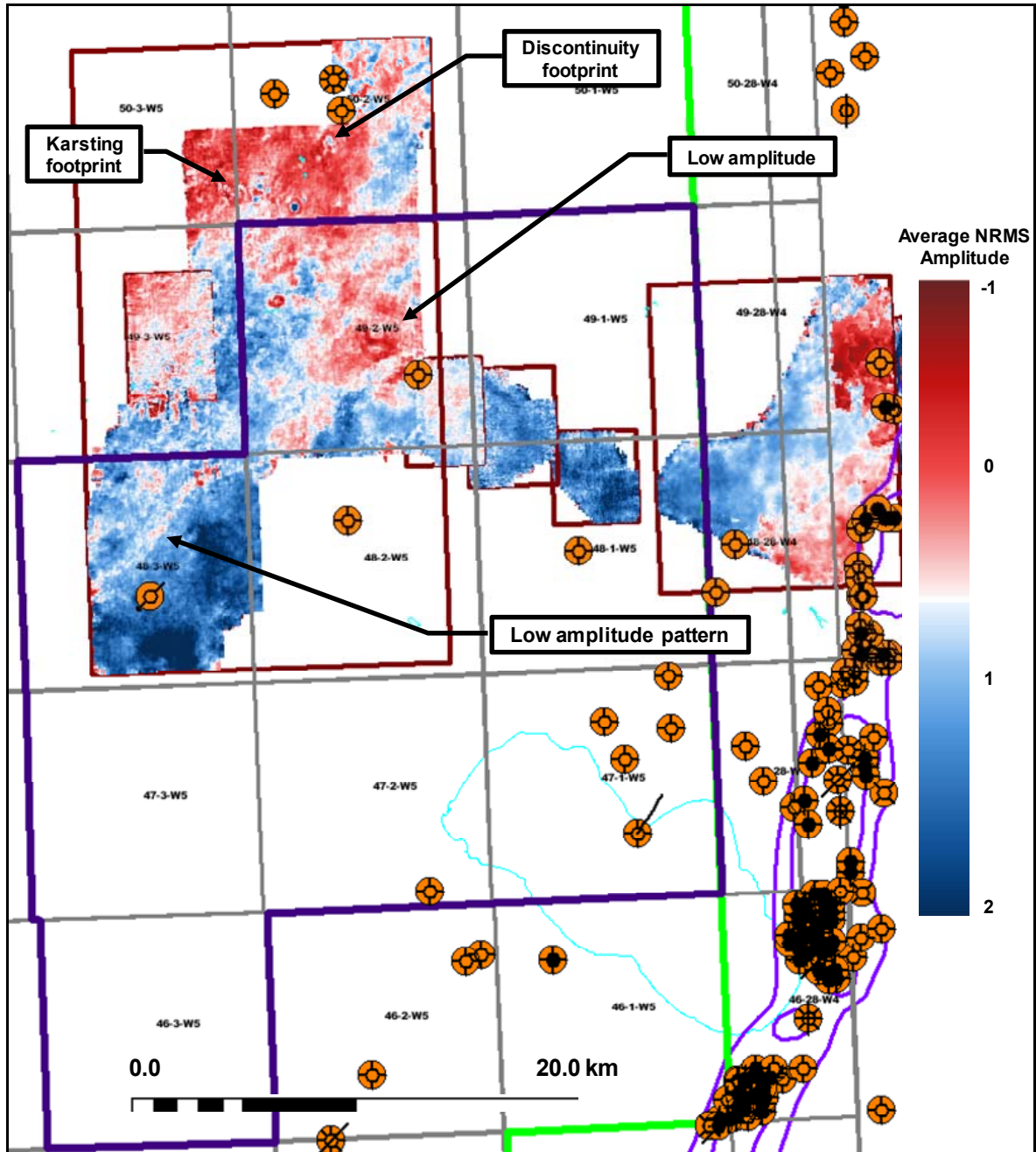


Figure 21: Average NRMS Nisku amplitude over a 10 ms window (centred on the Nisku horizon pick). In addition to the patterns already defined in the NRMS Nisku amplitude map (Section 4 and Figure 12), another low amplitude pattern emerges from the map. The NRMS amplitude averaging window of 10 ms seems appropriate except within the north-eastern region of the easternmost 3D volume. The relative position to the large study area is shown by the dashed rectangle in the base map in Figure 11.

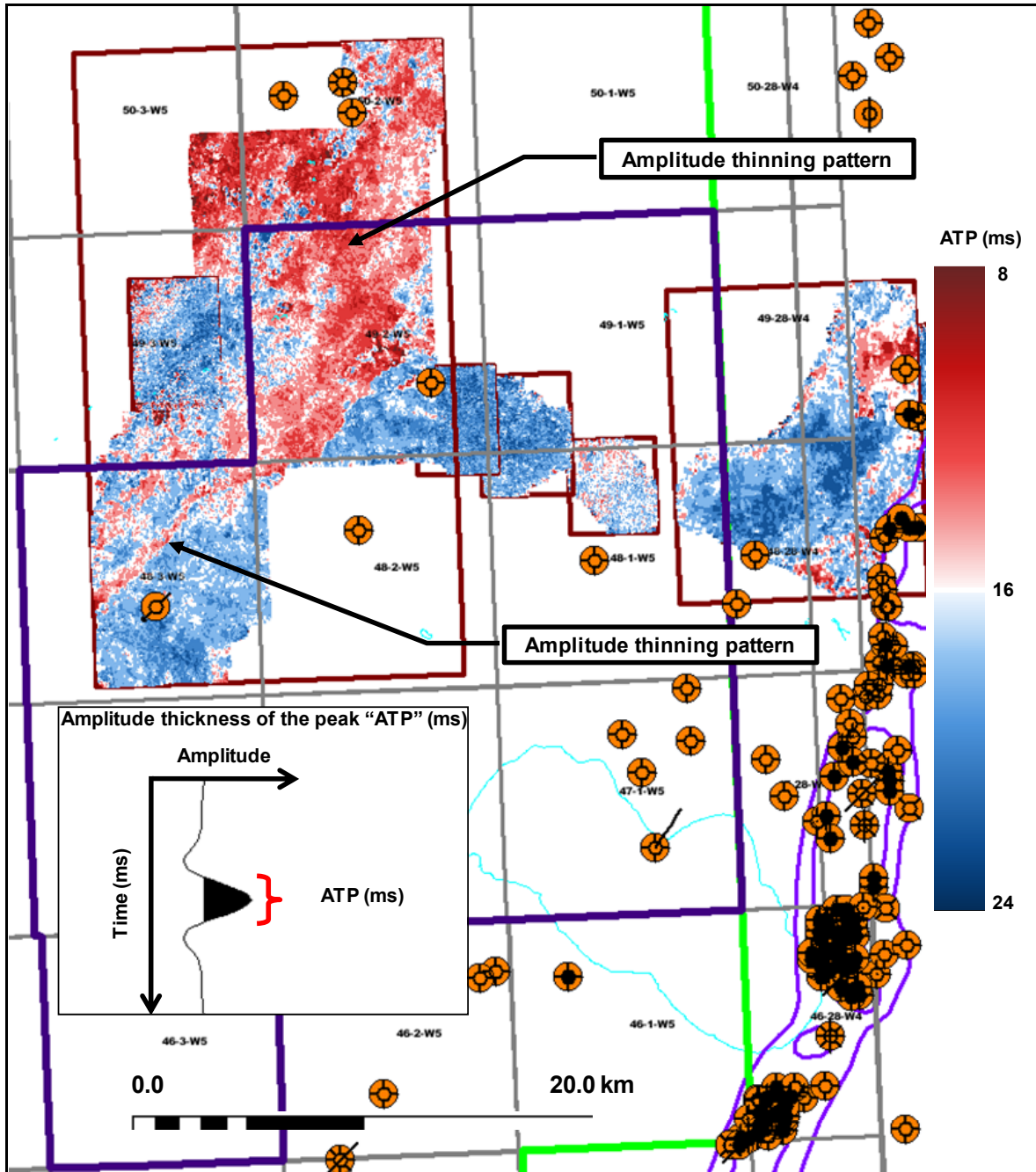


Figure 22: Amplitude thickness of the Nisku peak (ATP) in ms. The inset schematic illustrates the concept of ATP. Note the elongated (NE-SW) thinning pattern that is not captured by the NRMS amplitude map. See the multi-segment line in Figure 13 and 14 for a cross-sectional view of those anomalies. The relative position to the large study area is shown by the dashed rectangle in the base map in Figure 11.

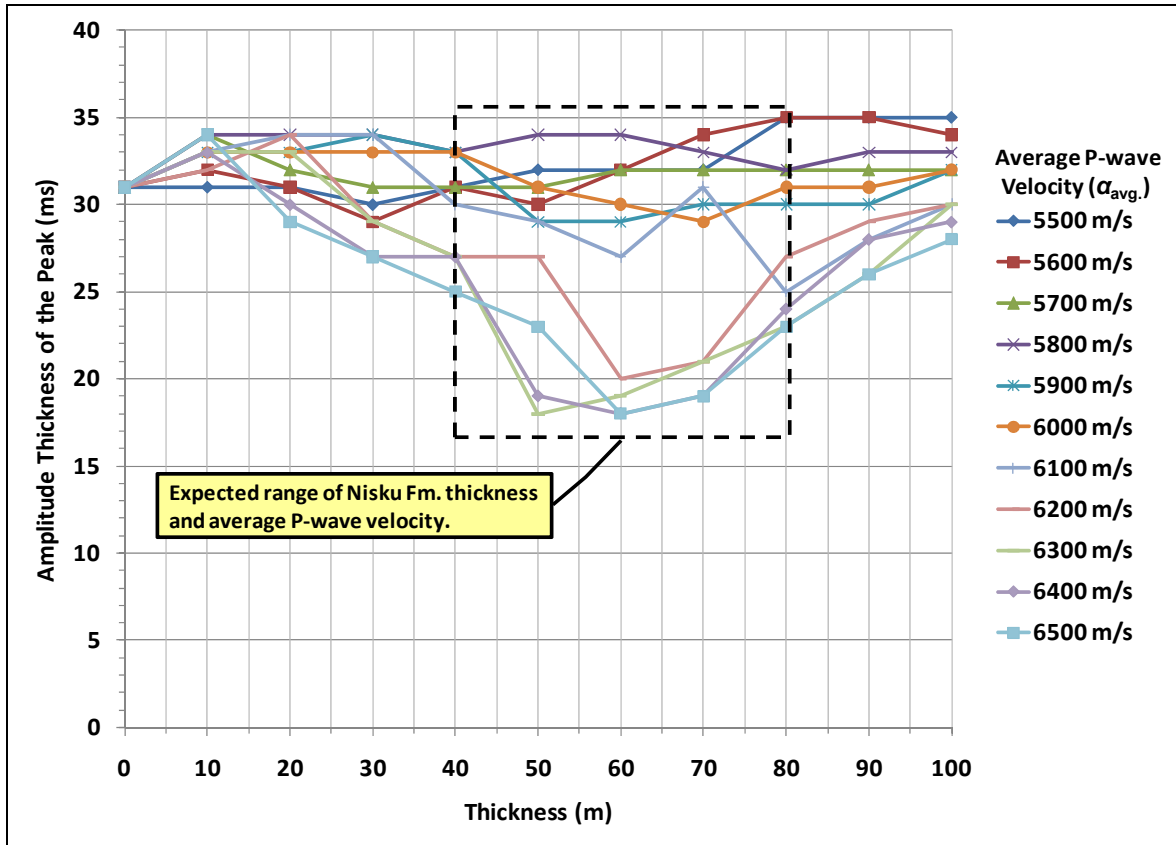


Figure 23: Amplitude thickness of the Nisku peak (ATP in ms) of the synthetic seismogram in Figure 17. The ATP is highly sensitive to variations in the Nisku Formation thickness and average P-wave velocity over the expected range of those parameters. There is a distinct separation in the velocity effect over the expected Nisku Formation thickness (~ 40 – 80 m). The separation seems to be occurring around the tuning thickness (~ 60 m) and the corresponding average P-wave velocity (~ 6100 m/s).

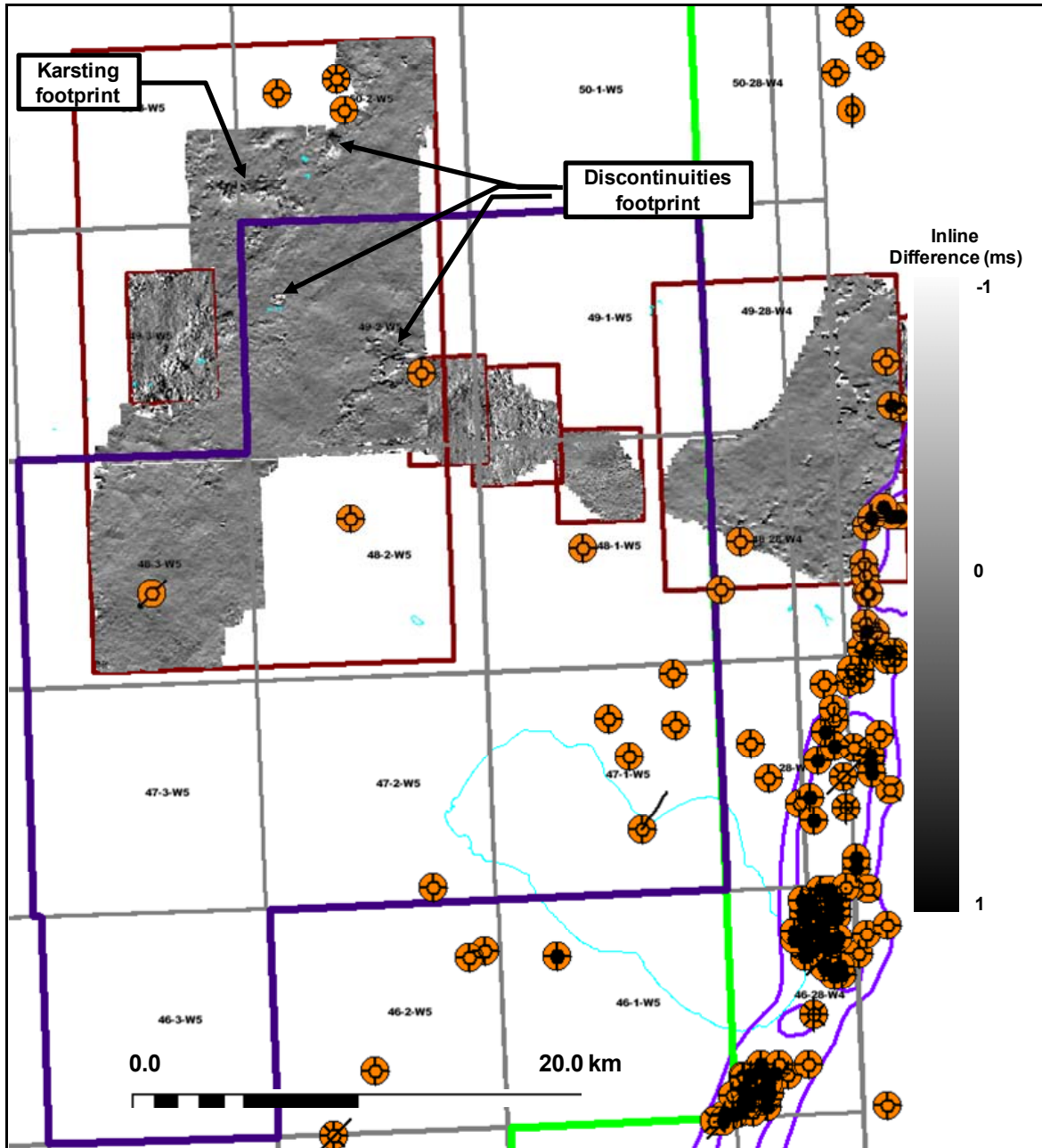


Figure 24: Inline difference (coherency) attribute of the Nisku event in ms. The difference method shows more sensitivity toward discontinuities within the Nisku compared with other seismic attributes as can be seen, for instance, with the Wabamun karsting effect on the Nisku event. See the multi-segment line in Figure 13 and 14 for a cross-sectional view of some of the identified anomalies. The relative position to the large study area is shown by the dashed rectangle in the base map in Figure 11.

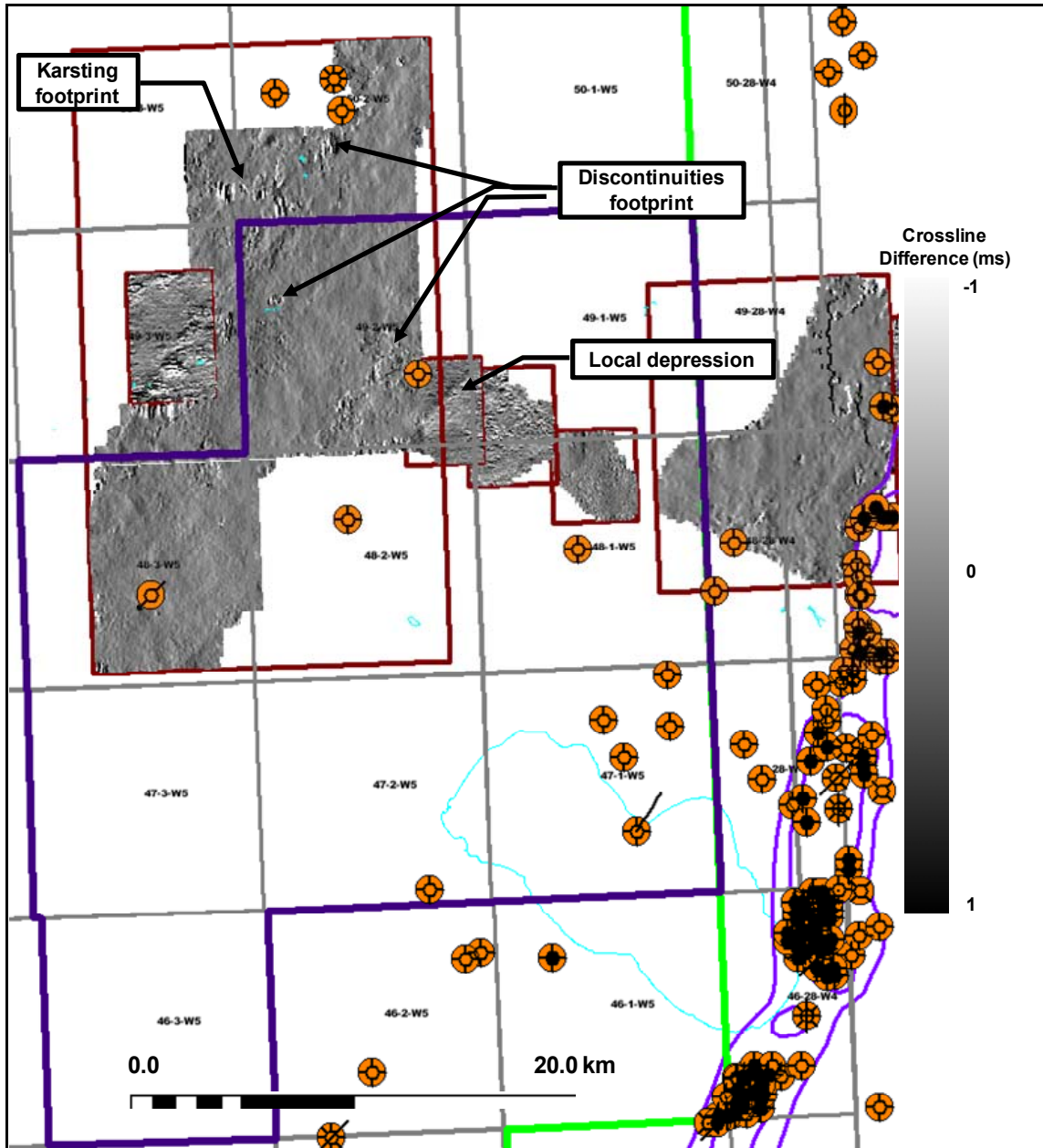


Figure 25: Crossline difference (coherency) attribute of the Nisku event in ms. Note the sensitivity, also, to the direction in which the difference is measured compared to the inline difference in Figure 24. The crossline difference was not as robust as the inline difference in defining geologic features within the reference 3D volume (e.g., the Wabamun karsting effect). However, it performed better in defining some of the features associated with other seismic volumes, such as the local time low (also shown in the time structure map in Figure 10). See the multi-segment line in (Figure 13 and 14) for a cross-sectional view of some of the identified anomalies. The relative position to the large study area is shown by the dashed rectangle in the base map in Figure 11.

8. ACOUSTIC IMPEDANCE INVERSION

Acoustic impedance is one of the most useful seismic attributes as it yields distribution of pseudo-physical properties rather than a set of observations pertaining to the physical properties distribution. However, acoustic impedance is more difficult to determine as it requires seismic inversion, which calls for good estimation of parameters as well as high quality seismic data and a good distribution of well control. Furthermore, inversion suffers from non-uniqueness.

In this project, various post-stack acoustic impedance inversion techniques were tested and only two were found to produce useful results: band-limited and model-based inversions. Band-limited inversion, also known as recursive inversion, is constrained mainly by the bandwidth of the seismic data, which typically falls between 7 and 60 Hz. The method estimates the acoustic impedance recursively by first extracting an estimate of the reflection coefficient from the seismic data and then re-arranging the normal incidence reflection coefficient relation to solve for the acoustic impedance of the $n^{\text{th}}+1$ layer (Z_{n+1}):

$$R_n = \frac{Z_{n+1} - Z_n}{Z_{n+1} + Z_n} \xrightarrow{\text{solving for } Z_{n+1}} Z_{n+1} = \frac{Z_n(1+R_n)}{1-R_n} \quad 3$$

Where R_n is the reflection coefficient of the n^{th} layer, Z_n is the acoustic impedance of the n^{th} layer ($\text{kg/m}^2\cdot\text{s}$), and n is a positive integer. Recall that the acoustic impedance of the n^{th} layer is its P-wave velocity (m/s) multiplied by its density (kg/m^3), i.e., $Z_n = \alpha_n \times \rho_n$ (Cooke and Schneider, 1983).

Model-based inversion uses a different approach. First, the well control and the seismic data (horizons) are used to build an initial low-frequency estimated model of the acoustic impedance distribution. Using an estimate of the source wavelet, the model is then perturbed and the model response, in the form of synthetic seismogram, is measured. The model responses are then compared to the actual seismic traces, usually by means of cross correlation. The process is iterated until the model converges, i.e., the model response becomes within a predefined acceptable range from the actual observation. The misfit error between the two is quantified through various means; one of the most commonly used measures is the sum of the squared differences (Lines and Treitel, 1984).

There are many elements that could degrade the reliability of the inversion results, some of which could not be controlled, such as noise, whereas others could not be precisely calculated, such as the source wavelet. However, each method has its own advantages and disadvantages in regard to those limitations and it is suggested that by using both methods some of the ambiguities associated with the inversion results could be minimized. More information about those and other inversion methods can be found in Waters (1978), Aki and Richards (1980), Lines and Treitel (1984), Russell (1988), and the STRATA software theory manual.

Figure 26 depicts some of the major steps adopted in the acoustic impedance inversion framework. A critical factor to achieving good inversion results is the seismic-to-well tie. The correlation coefficients associated with the wells used in the inversion are shown in Table 4. Prior to showing the Nisku acoustic impedance map, two examples were selected to illustrate the performance of each of the inversion methods. The first example is from the 2D seismic line near the water source well (Figure 27) while the other is from an inline extracted from the reference 3D volume (Figure 30). Figures 28 and 31 show the initial “guessed” model for the 2D data and the extracted inline

seismic sections while the inversion results using band-limited and model-based inversion for those two sections are illustrated in Figure 29 and 32, respectively.

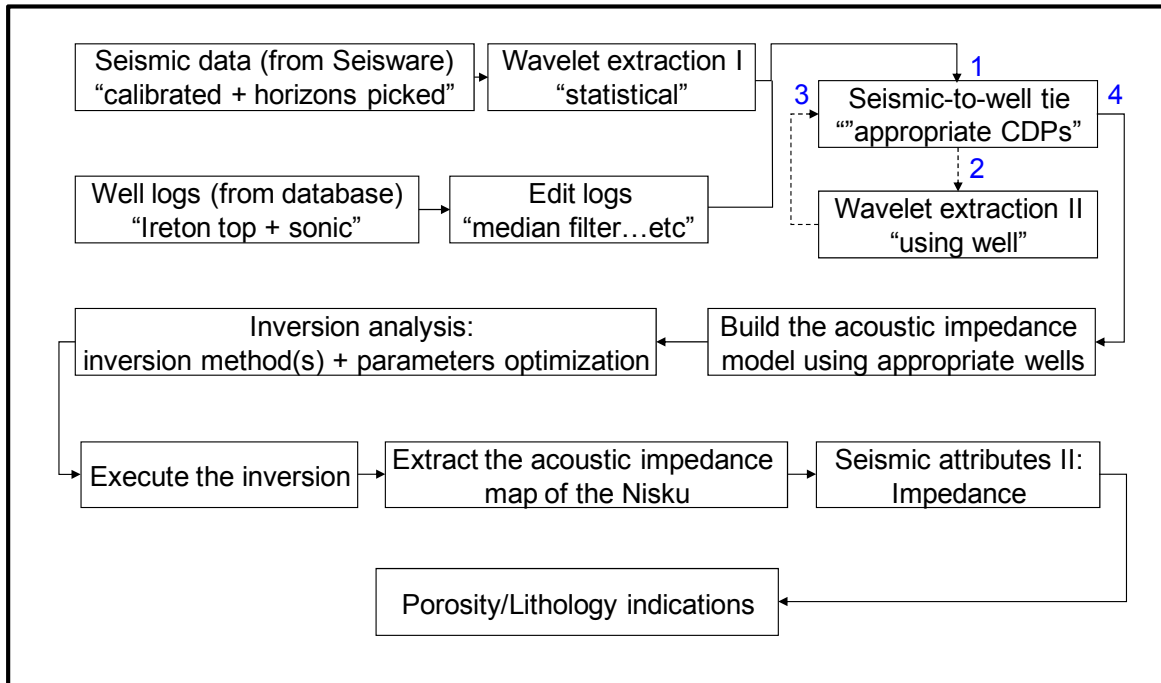


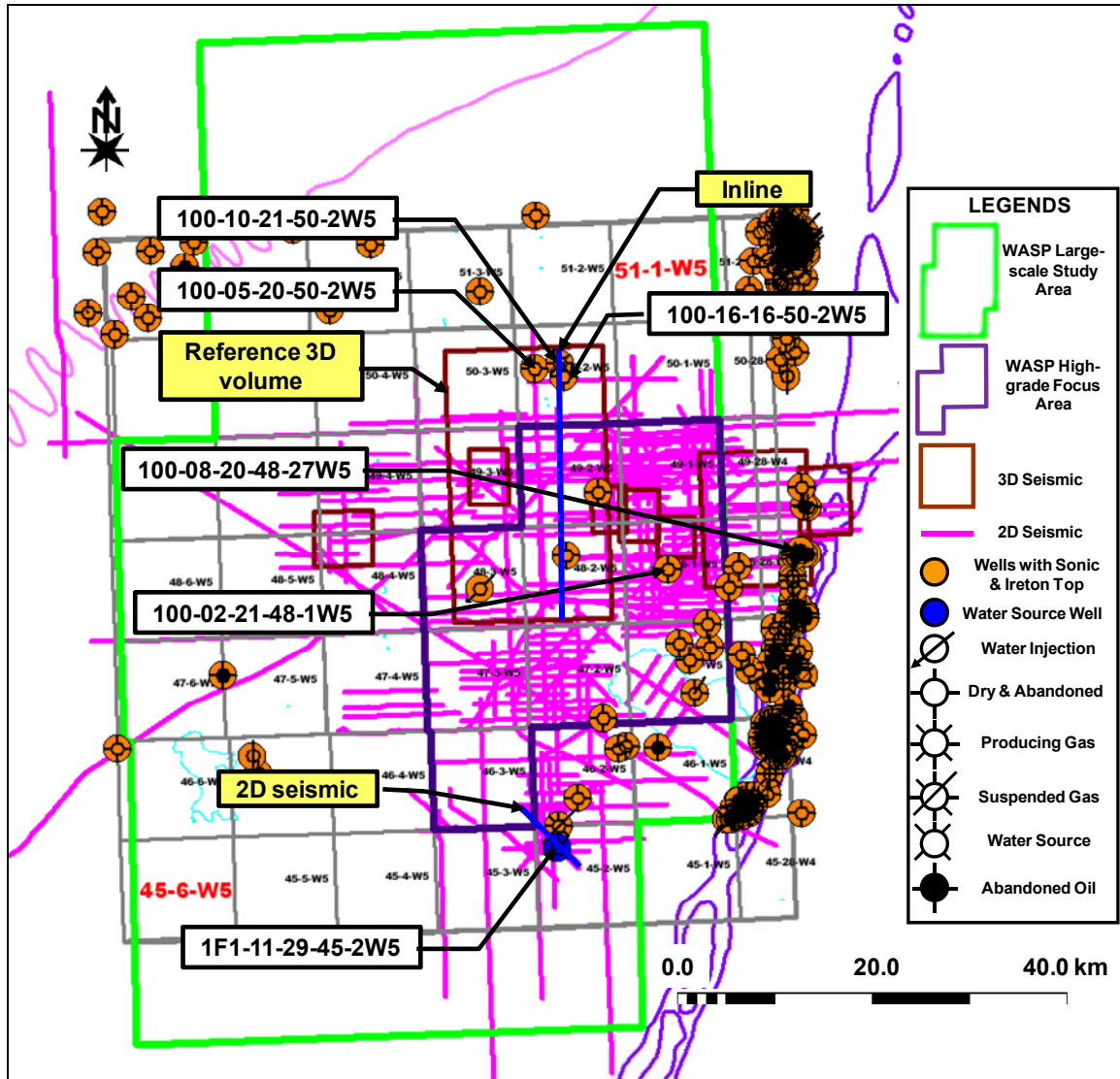
Figure 26: Flowchart outlining the major steps followed in the seismic inversion to extract the acoustic impedance map of the Nisku event.

The band-limited inversion appears to produce a more detailed acoustic impedance model than the model-based inversion. For instance, the Wabamun and the Nisku formations are clearly separated by low impedance in the band-limited inversion whereas they are hardly separated in the model-based inversion results (Figures 29 and 32). However, for the acoustic impedance of the Nisku Formation, both methods yield similar results (Figures 33 and 34), the only apparent difference being in the magnitude of the impedance. This is probably due to scaling differences. Furthermore, because there is a lack of well control, it is crucial that the impedance maps are interpreted only in terms of relative rather than absolute changes in acoustic impedance.

Several interesting low impedance zones are highlighted in Figures 33 and 34. The impedance determination from the 2D seismic line near the water source well is also shown for comparison. By examining those maps, there seems to be two categories of low impedance: one that is associated with lithological changes in the Nisku Formation and another which is associated with discontinuities in the overlying Wabamun event. A useful way to differentiate between those two classes is to use the difference attribute in Figure 24 and Figure 25. Any low acoustic impedance that cross-correlates between the impedance and the difference attributes is likely to be associated with Wabamun event discontinuities. With respect to the lithological changes, low acoustic impedance (Figures 33 and 34) appears to normally correspond to low NRMS and low average NRMS amplitude (Figure 12 and 21).

To relate variations in the acoustic impedance to the two primary physical parameters of interest, i.e., thickness and average P-wave velocity, the acoustic impedance model for the synthetic seismogram in Figure 17 was reconstructed using band-limited and model-based inversion methods (Figure 35). As with the amplitude modelling, variations in the average P-wave velocity seems to be the primary factor shaping the extracted acoustic impedance of the Nisku Formation.

Table 4: Correlation coefficient (over a designed correlation window) between seismic data and synthetic seismogram from selected wells within the study area. The well locations are shown in the base map. The blue lines show the location of the 2D seismic (Figure 27) and the inline (Figure 30) invoked in the inversion.



Well	Seismic Reference	Correlation Coefficient
1F1-11-29-45-2W5	2D	0.92
100-10-21-50-2W5	3D	0.80
100-16-16-50-2W5	3D	0.83
100-05-20-50-2W5	3D	0.72
100-02-21-48-1W5	3D	0.63
100-08-20-48-27W4	3D	0.80

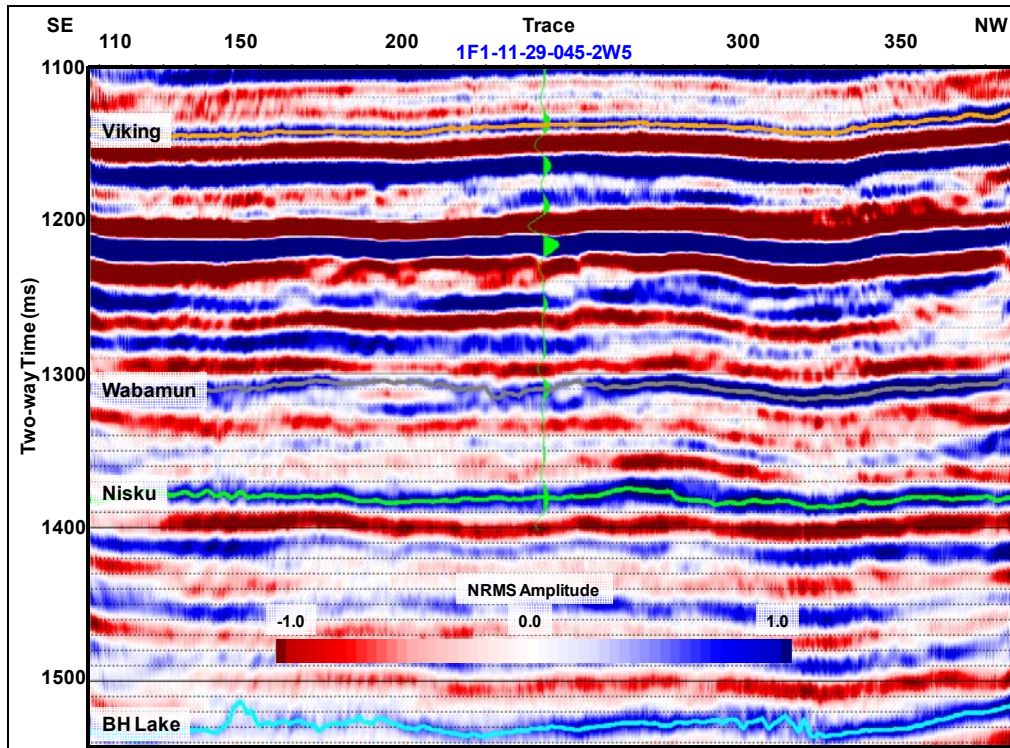


Figure 27: Seismic section near the water source well (Figure 3 and Table 4). The green curve at the well location is the correlated synthetic seismic trace. The correlation coefficient is 0.92.

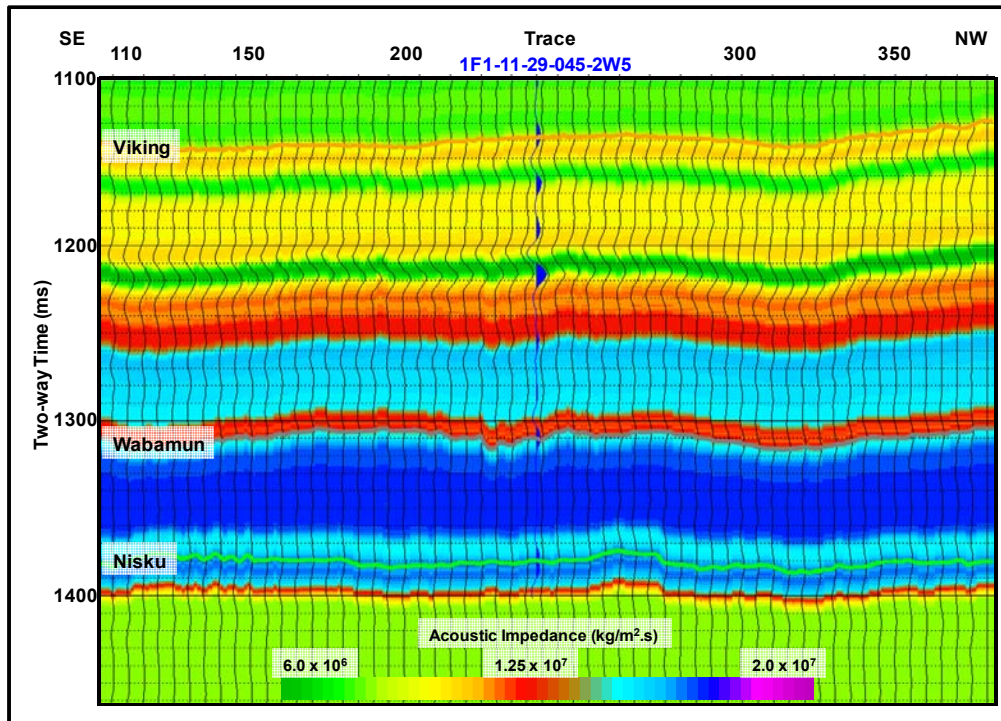


Figure 28: The initial acoustic impedance model. The blue curve at the well location is the correlated synthetic seismic trace while the black curves are the actual seismic traces.

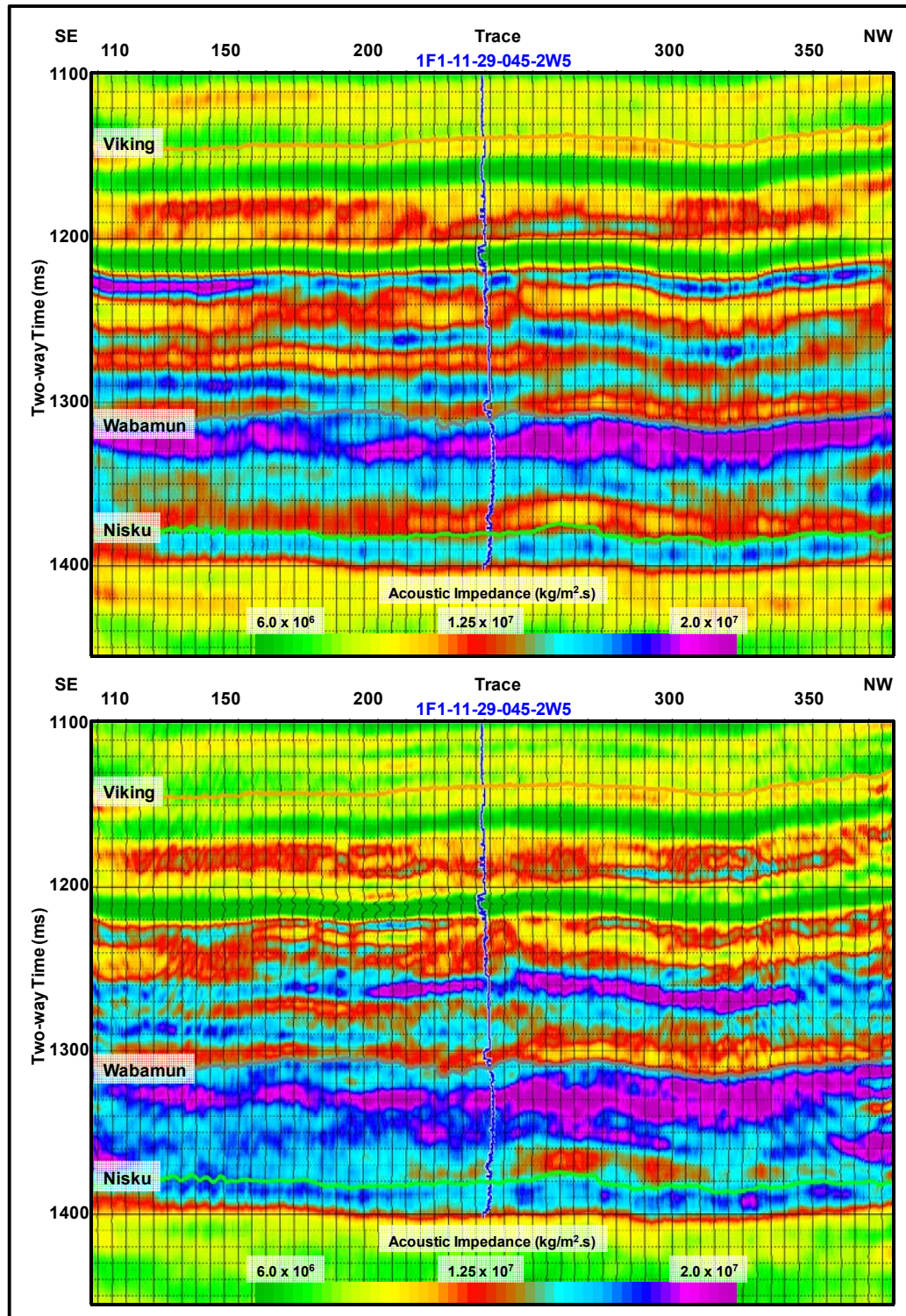


Figure 29: Estimated acoustic impedance along the 2D seismic line near the water source well (Figure 3) using band-limited (top) and model-based (bottom) inversion methods. The inserted blue curve at the well location represents the computed acoustic impedance from the sonic and density logs. The black curves represent the acoustic impedance from the band-limited inversion whereas in the model-based inversion they represent the misfit error.

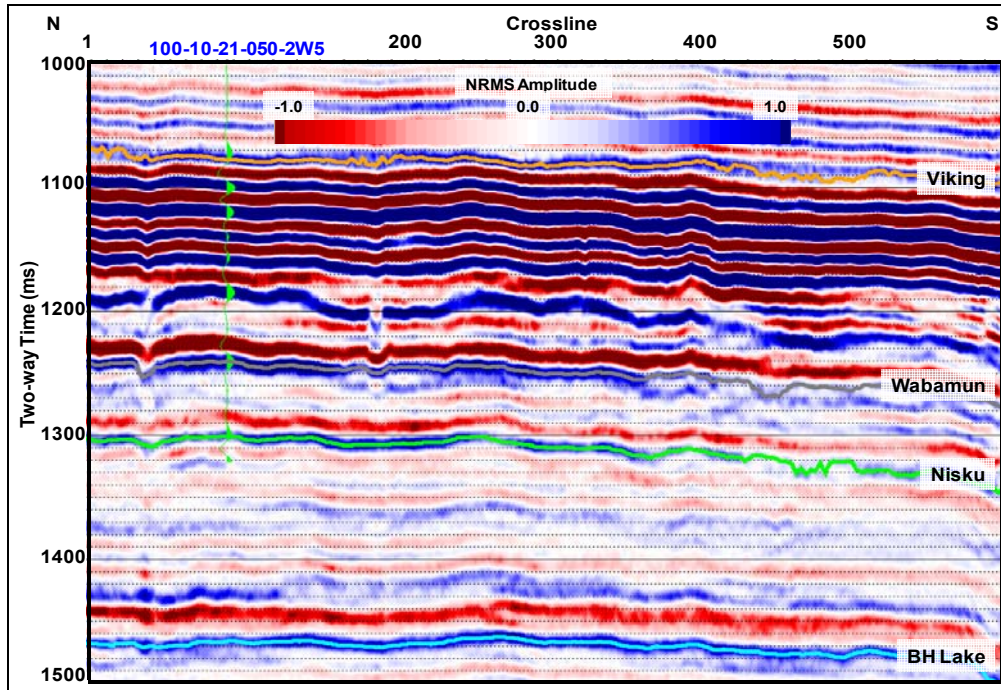


Figure 30: Inline extracted from the reference 3D seismic volume (Table 4). The green curve at the well location is the correlated synthetic seismic trace. The correlation coefficient is 0.80.

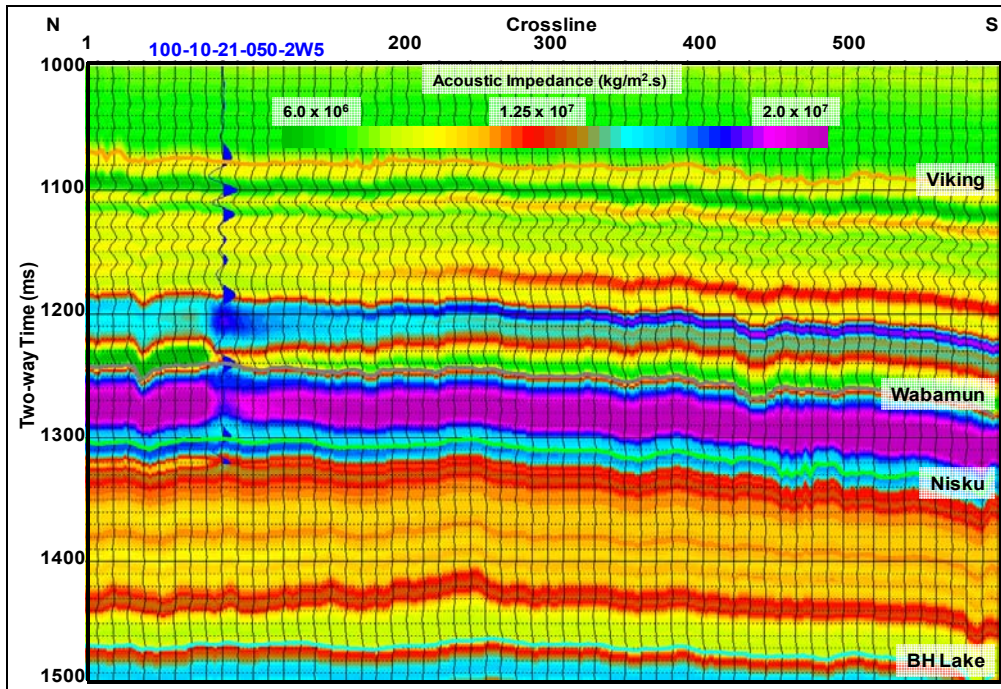


Figure 31: The initial acoustic impedance model corresponding to the inline in Figure 30. The blue curve at the well location is the correlated synthetic seismic trace while the black curves are the actual seismic traces.

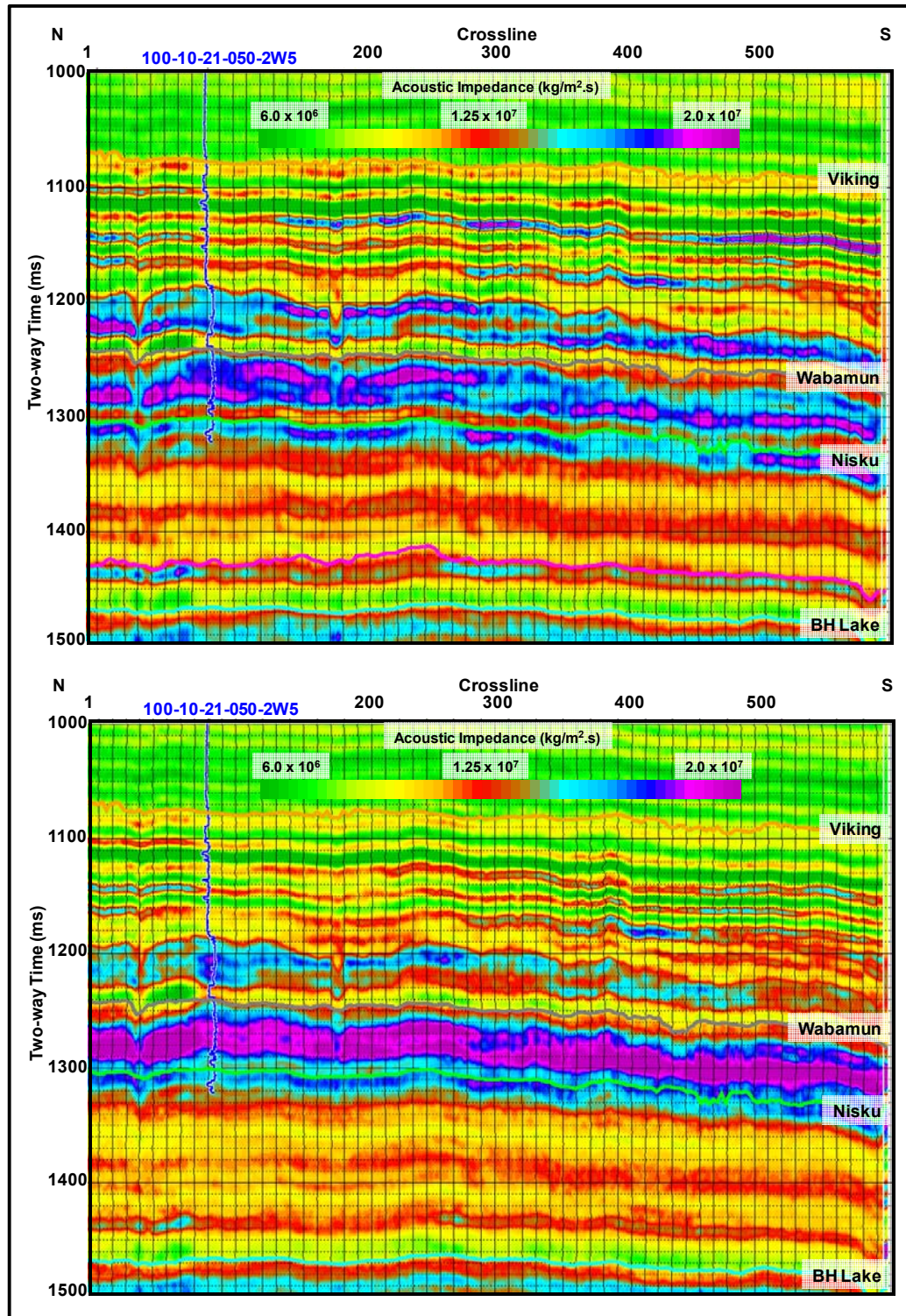


Figure 32: Estimated acoustic impedance of the inline in Figure 30 and Figure 31 using band-limited (top) and model-based (bottom) inversion methods. The inserted blue curve at the well location represents the computed acoustic impedance from the sonic and density logs. The black curves refer to the acoustic impedance from the band-limited inversion whereas in the model-based inversion they represent the misfit error.

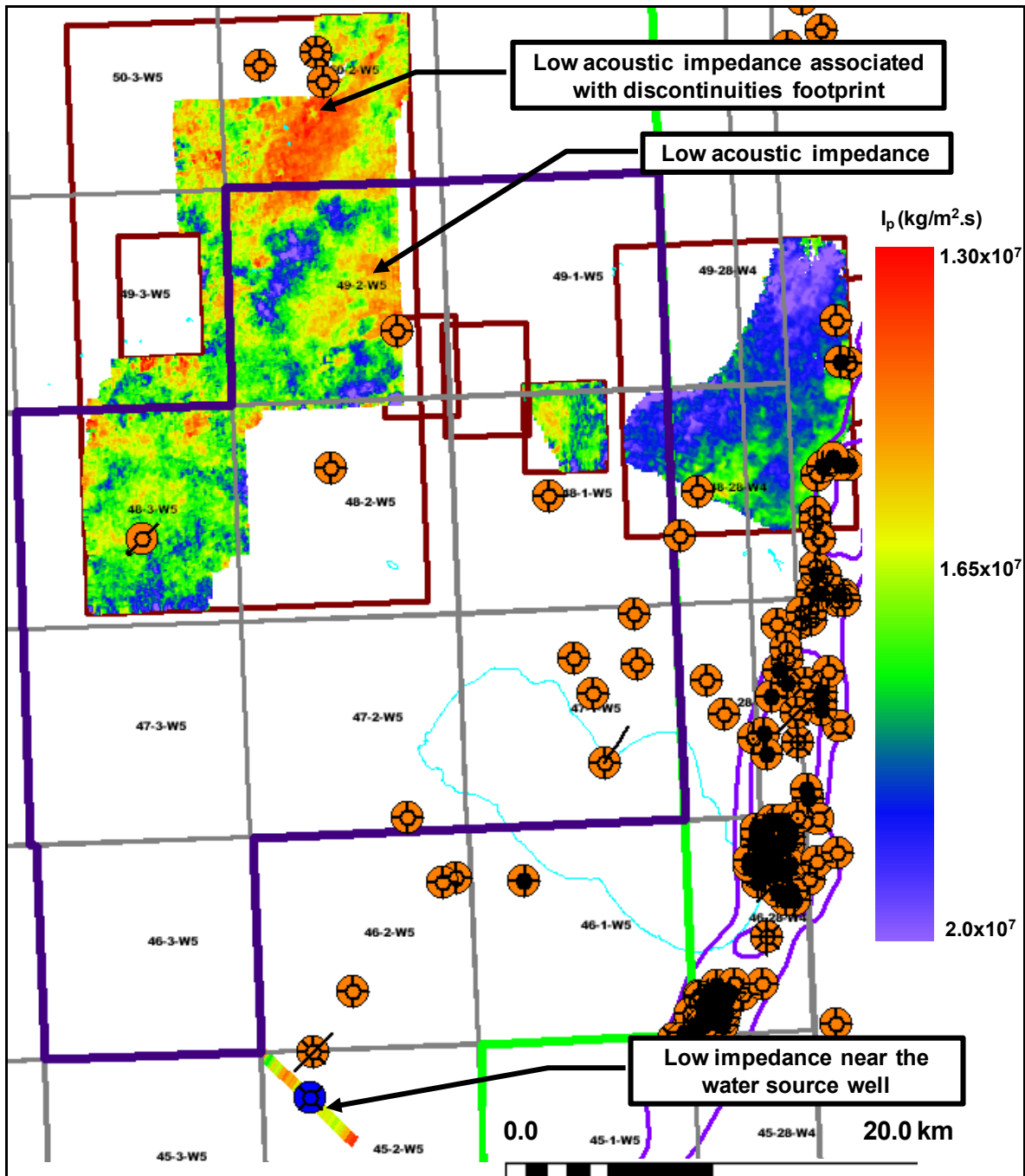


Figure 33: Estimated Acoustic impedance (I_p) map of the Nisku Formation using band-limited inversion. Due to lack of well control, the inversion was not performed on the entire dataset. The relative position to the large study area is shown by the dashed rectangle in the base map in Figure 11.

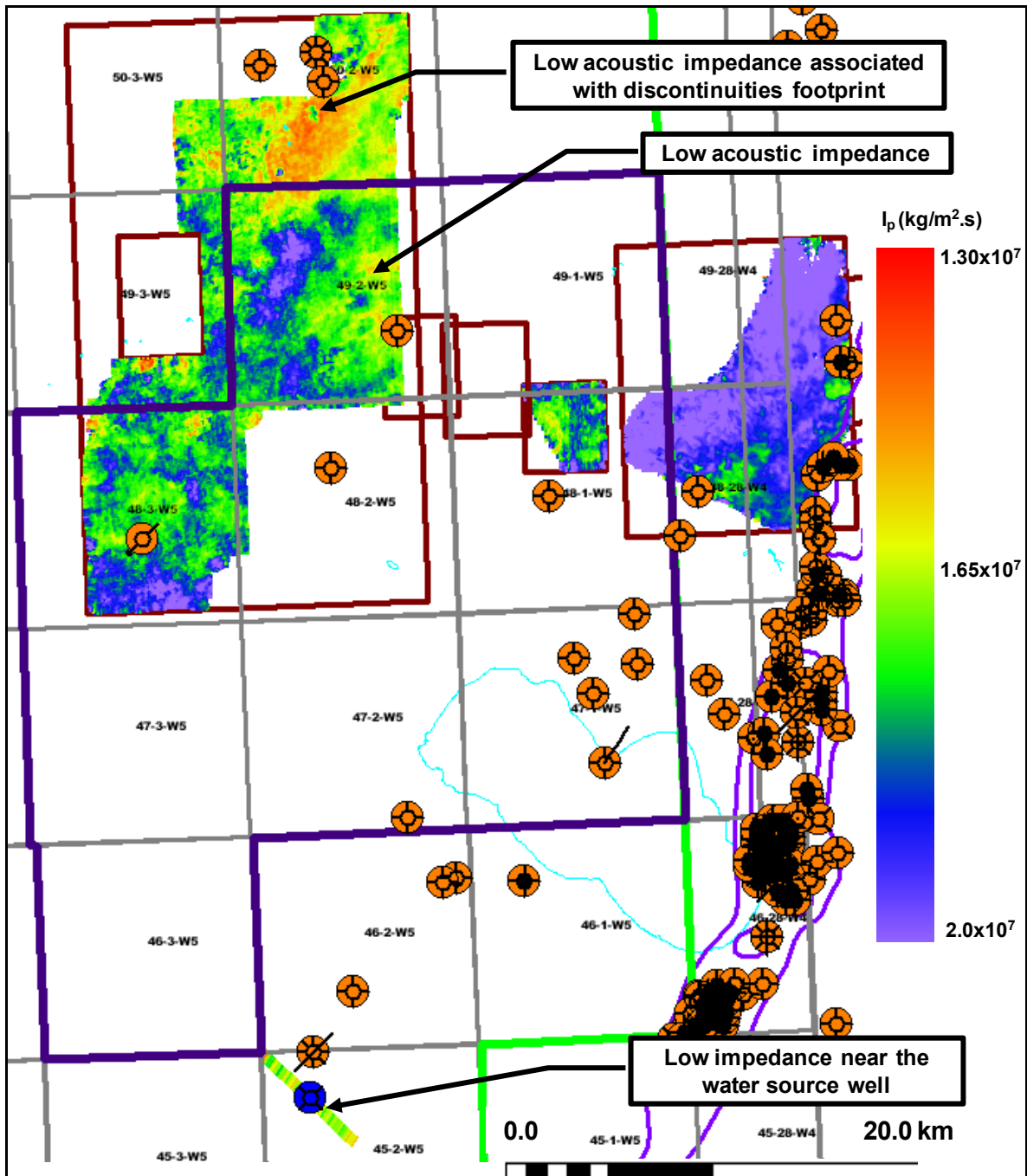


Figure 34: Estimated Acoustic impedance (I_p) map of the Nisku Formation using model-based inversion. Due to lack of well control, the inversion was not performed on the entire dataset. The relative position to the large study area is shown by the dashed rectangle in the base map in Figure 11.

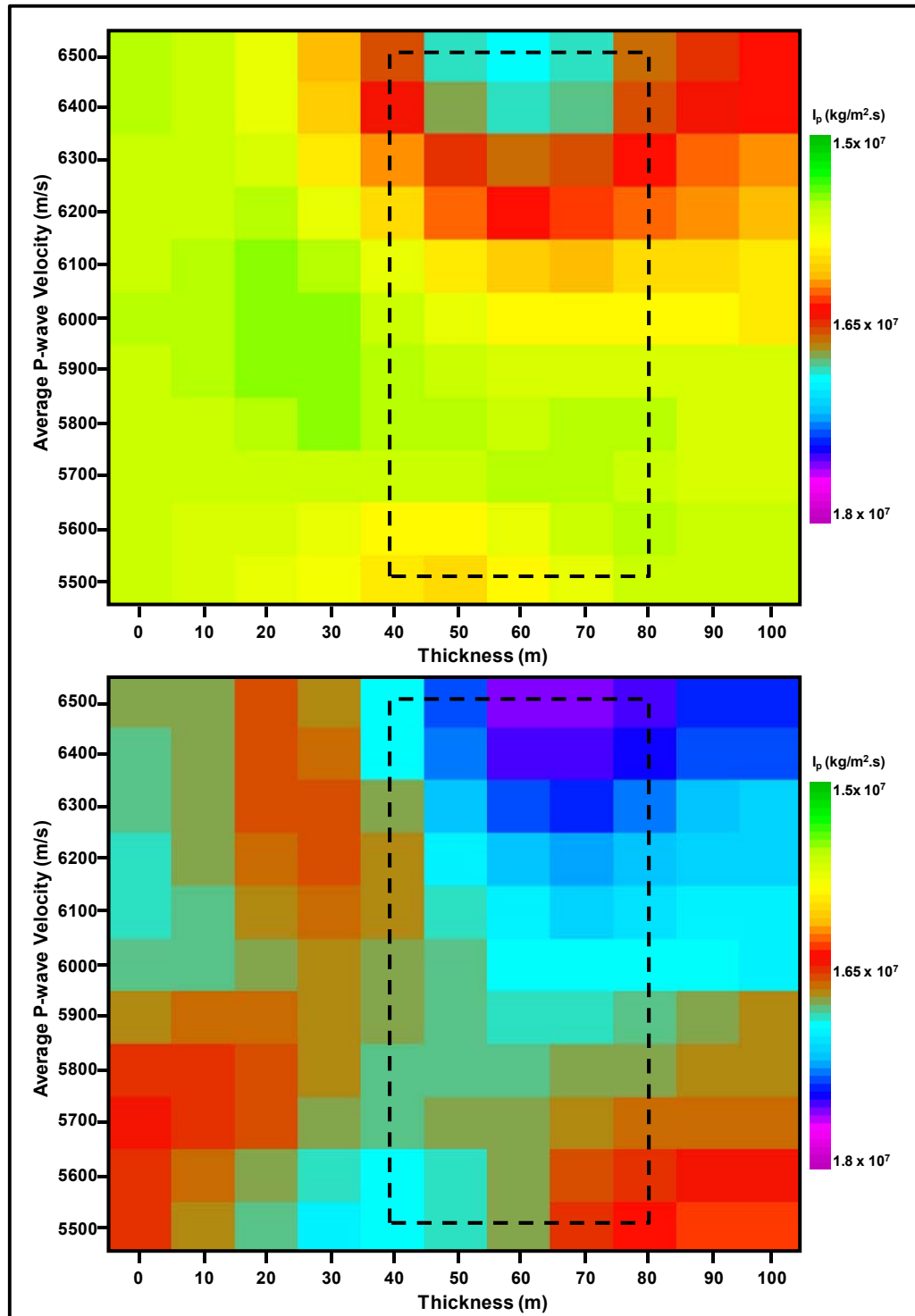


Figure 35: Acoustic impedance (I_p) of the synthetic seismogram in Figure 17 using band-limited (top) and model-based (bottom) inversion methods. Similar to the seismic amplitude response, the acoustic impedance shows high sensitivity toward variations in the Nisku Formation average P-wave velocity rather than thickness. The maps illustrate the direct proportionality between average P-wave velocity and acoustic impedance. Note the similarity in the results except for the small difference in the magnitude of the acoustic impedance due to scaling issues.

9. POROSITY ESTIMATION

Using the P-wave velocity derived from the band-limited acoustic impedance inversion, the bulk porosity of the Nisku Formation was estimated by invoking Wylie's (1956) time-average equation, which states that:

$$\frac{1}{\alpha_{bulk}} = \frac{(1 - \phi)}{\alpha_{matrix}} + \frac{\phi}{\alpha_{fluid}} \quad 4$$

where ϕ is the porosity (dimensionless), α_{matrix} is P-wave velocity of the Nisku matrix (assumed to be ≈ 6800 m/s), α_{fluid} is the P-wave velocity of the Nisku pore fluid (brine ≈ 1600 m/s), and α_{bulk} is the Nisku bulk P-wave velocity (m/s) derived from the band-limited acoustic impedance inversion. Re-arranging equation (4) and solving for porosity (ϕ):

$$\phi = \frac{\alpha_{fluid} [\alpha_{matrix} - \alpha_{bulk}]}{\alpha_{bulk} [\alpha_{matrix} - \alpha_{fluid}]} \quad 5$$

The resultant pseudo-porosity map in Figure 36 correlates fairly well with the low impedance zones in Figures 33 and 34, which is expected since the bulk velocity (α_{bulk}) used in estimating the porosity is derived from the acoustic impedance itself. Although Wylie's time-average equation assumes clean consolidated formations with uniformly distributed pores (Sherriff, 1991), the estimated porosity values seem to fall within the expected range based on wireline data (resistivity log) and core analysis.

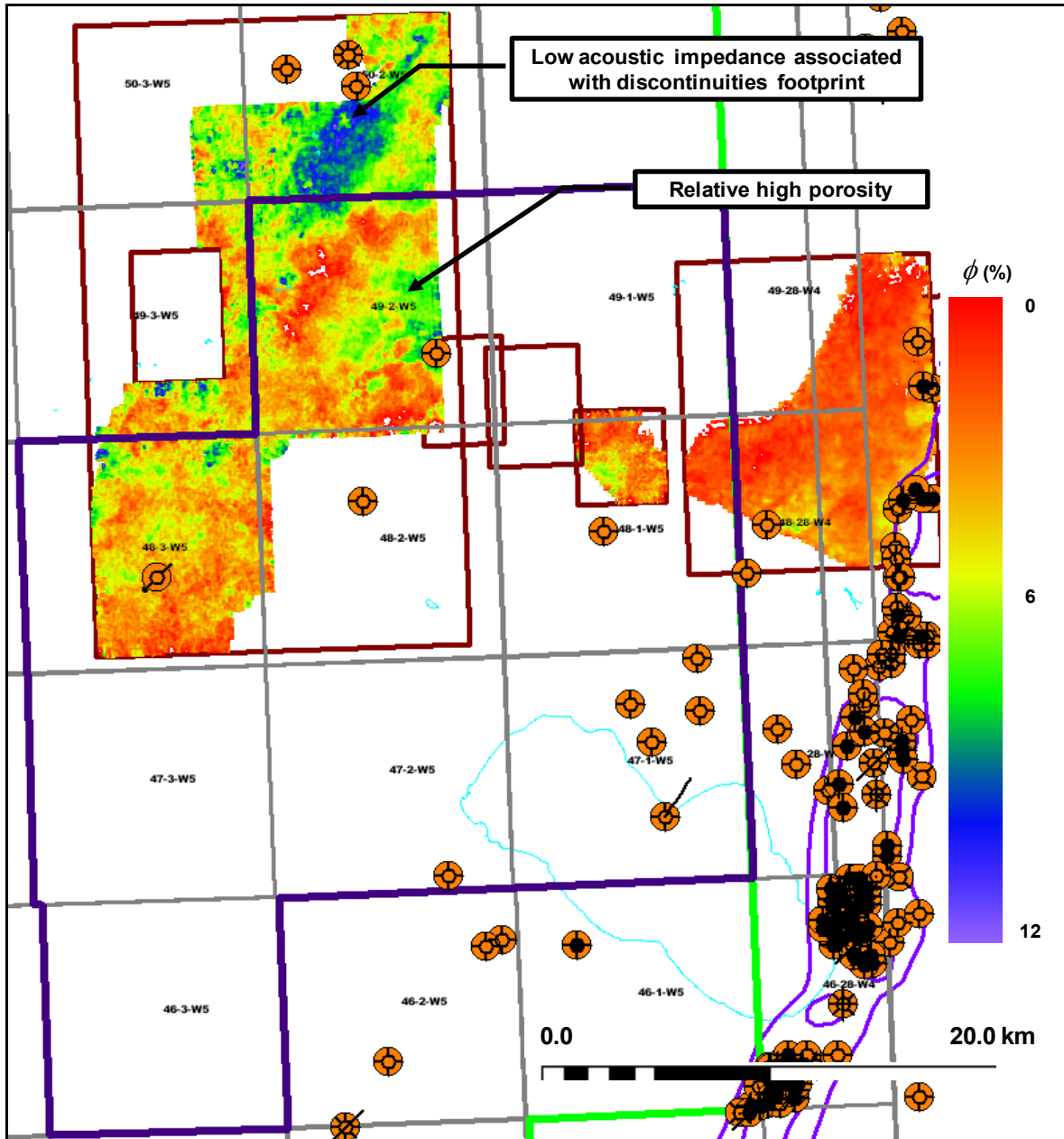


Figure 36: Estimated bulk porosity of the Nisku event using Wylie’s time-average equation with bulk velocity derived from the band-limited acoustic impedance inversion. The relative position to the large study area is shown by the dashed rectangle in the base map in Figure 11.

10. ROCK PHYSICS: FLUID REPLACEMENT MODELLING

Understanding the seismic response to fluid changes within the Nisku Formation is crucial to success of any time-lapse seismic monitoring that may be implemented as part of a measurement, monitoring and verification (MMV) program associated with carbon capture and storage in the study area. Therefore, fluid replacement modelling (FRM) was undertaken to estimate changes in the rock elastic moduli that would result if the original pore-filling fluid in the rock (i.e., brine) is replaced with another fluid (i.e., supercritical CO₂). In our modelling, we invoked the Gassmann (1951) approach. Wang (2001) and Smith et al. (2003) provide a good overview of the Gassmann method and the underlying assumptions. In a concise form, the Gassmann's equation states that:

$$K_{\text{saturated}}^{\text{fluid 1}} = K_{\phi} + \frac{\left(1 - \frac{K_{\phi}}{K_{\text{mineral}}}\right)^2}{\left(\frac{\phi}{K_{\text{fluid}}^{\text{fluid 1}}} + \frac{(1-\phi)}{K_{\text{mineral}}} - \frac{K_{\phi}}{(K_{\text{mineral}})^2}\right)}$$

6

Where:

$K_{\text{saturated}}^{\text{fluid 1}}$ is the bulk modulus of the rock (saturated with the initial fluid) in GPa.

K_{ϕ} is the bulk modulus of the porous rock frame in GPa.

K_{mineral} is the bulk modulus of the rock mineral matrix GPa.

$K_{\text{fluid}}^{\text{fluid 1}}$ is the bulk modulus of the pore-filling (initial) fluid GPa.

ϕ is the porosity (dimensionless).

The bulk modulus of the rock with the initial saturation ($K_{\text{saturated}}^{\text{fluid 1}}$) is given by:

$$K_{\text{saturated}}^{\text{fluid 1}} = \rho_{\text{saturated}}^{\text{fluid 1}} \left[\left(\alpha_{\text{saturated}}^{\text{fluid 1}}\right)^2 - \frac{3}{4} \left(\beta_{\text{saturated}}^{\text{fluid 1}}\right)^2 \right]$$

7

Where the S-wave velocity $\beta_{\text{saturated}}^{\text{fluid 1}}$ is related to the shear modulus $\mu_{\text{saturated}}^{\text{fluid 1}}$ through:

$$\mu_{\text{saturated}}^{\text{fluid 1}} = \rho_{\text{saturated}}^{\text{fluid 1}} \left(\beta_{\text{saturated}}^{\text{fluid 1}}\right)^2 \Rightarrow \beta_{\text{saturated}}^{\text{fluid 1}} = \sqrt{\frac{\mu_{\text{saturated}}^{\text{fluid 1}}}{\rho_{\text{saturated}}^{\text{fluid 1}}}}$$

8

The density $\rho_{\text{saturated}}^{\text{fluid 1}}$ is calculated through the relation:

$$\rho_{\text{saturated}}^{\text{fluid 1}} = \phi \rho_{\text{fluid}}^{\text{fluid 1}} + (1-\phi) \rho_{\text{mineral}}$$

9

Where $\rho_{\text{fluid}}^{\text{fluid 1}}$ is the density of the initial fluid (i.e., brine), and ρ_{mineral} is the density of the matrix (i.e., dolostone). The necessary parameters (P-wave velocity [$\alpha_{\text{saturated}}^{\text{fluid 1}}$], S-wave velocity [$\beta_{\text{saturated}}^{\text{fluid 1}}$], density [$\rho_{\text{saturated}}^{\text{fluid 1}}$] and porosity [ϕ]) required to solve for equation (6) are usually estimated using

wireline data (in our modelling we used the data from the water source well 1F1-11-29-45-2W5 shown in Figure 3). One of the key aspects of the Gassmann method is that K_ϕ remains unchanged regardless of the fluid with which the rock is saturated. Thus, the next major step is to re-arrange the above equation to solve for (K_ϕ):

$$K_\phi = \frac{K_{\text{saturated}}^{\text{fluid 1}} \left(\frac{\phi K_{\text{mineral}}}{K_{\text{fluid}}^{\text{fluid 1}}} + 1 - \phi \right)}{\left(\frac{\phi K_{\text{mineral}}}{K_{\text{fluid}}^{\text{fluid 1}}} + \frac{K_{\text{saturated}}^{\text{fluid 1}}}{K_{\text{mineral}}} - 1 - \phi \right)} \quad 10$$

So once it is known, then it is possible to saturate the system with a replacement fluid ($K_{\text{fluid}}^{\text{fluid 2}}$) and thus calculate the resultant bulk modulus ($K_{\text{saturated}}^{\text{fluid 2}}$):

$$K_{\text{saturated}}^{\text{fluid 2}} = K_\phi + \frac{\left(1 - \frac{K_\phi}{K_{\text{mineral}}} \right)^2}{\left(\frac{\phi}{K_{\text{fluid}}^{\text{fluid 2}}} + \frac{(1-\phi)}{K_{\text{mineral}}} - \frac{K_\phi}{(K_{\text{mineral}})^2} \right)} \quad 11$$

Where:

$K_{\text{saturated}}^{\text{fluid 2}}$ is the bulk modulus of the rock (saturated with the new fluid) in GPa.
 $K_{\text{fluid}}^{\text{fluid 2}}$ is the bulk modulus of the pore-filling (new) fluid GPa.

Finally, the bulk and shear moduli of the new system are used to calculate the new P-wave ($\alpha_{\text{saturated}}^{\text{fluid 2}}$) and S-wave ($\beta_{\text{saturated}}^{\text{fluid 2}}$) velocities, and subsequently, the acoustic impedance:

$$\alpha_{\text{saturated}}^{\text{fluid 2}} = \sqrt{\frac{\frac{4}{3} K_{\text{saturated}}^{\text{fluid 2}} + \mu_{\text{saturated}}^{\text{fluid 2}}}{\rho_{\text{saturated}}^{\text{fluid 2}}}} \quad 12$$

$$\beta_{\text{saturated}}^{\text{fluid 2}} = \sqrt{\frac{\mu_{\text{saturated}}^{\text{fluid 2}}}{\rho_{\text{saturated}}^{\text{fluid 2}}}} \quad 13$$

Note that the shear modulus is assumed to be insensitive to fluid properties and therefore:

$$\mu_{\text{saturated}}^{\text{fluid 1}} = \mu_{\text{saturated}}^{\text{fluid 2}}$$

The density of the new saturated system ($\rho_{\text{saturated}}^{\text{fluid 2}}$) is calculated through the relation:

$$\rho_{\text{saturated}}^{\text{fluid 2}} = \phi S_w \rho_{\text{fluid 1}}^{\text{fluid 1}} + \phi(1 - S_w) \rho_{\text{fluid 2}}^{\text{fluid 2}} + (1 - \phi) \rho_{\text{mineral}}$$
14

where S_w is the water saturation, and $\rho_{\text{fluid 2}}^{\text{fluid 2}}$ is the density of the new fluid (i.e., CO₂). For the FRM, the following constituents were selected for the modelling:

1. Dolostone as the single mineralogy of which the rock matrix is comprised (mineral).
2. Brine as the initial fluid with which the pore space is filled (fluid 1).
3. Supercritical carbon dioxide (CO₂) as the new fluid being introduced into the reservoir (fluid 2).

The values and ranges selected for the above constituents are given in Table 5. The results obtained using those parameters and the fluid substitution method discussed above suggest that changes in the average acoustic impedance is rather small and the change in the shear impedance is insignificant as a function of increasing CO₂ saturation (Figure 37).

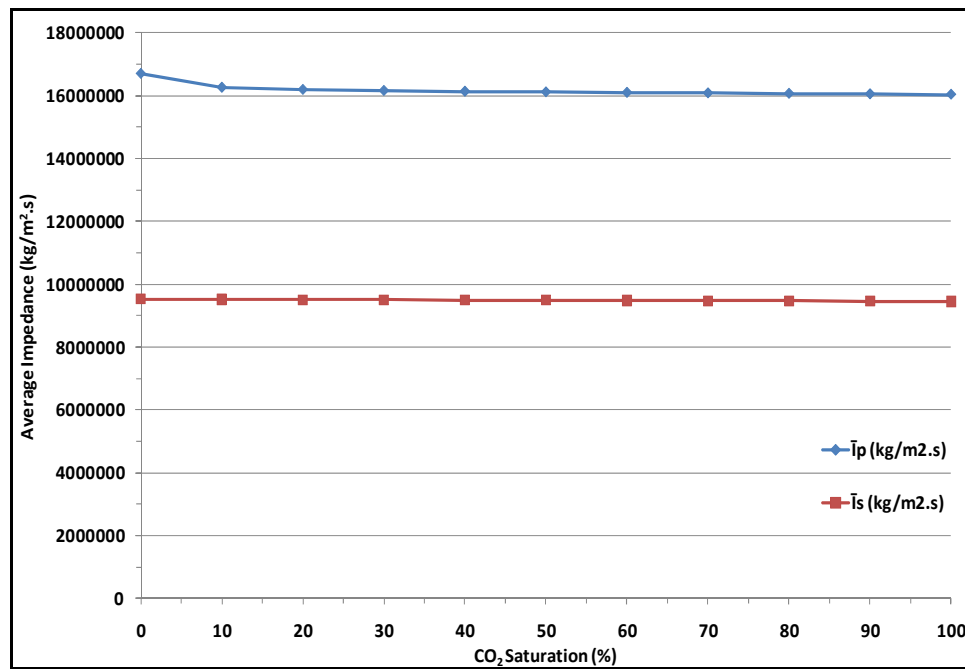
Table 5: Parameters pertaining to the main constituents in the Gassmann FRM. The pressure, temperature, porosity and thickness of the Nisku Formation were 15 MPa, 50.3 Co, 9%, and 56 m respectively (Michael et al., 2008). Salinity and viscosity were adopted from Michael et al. (2008) whereas the rest of the parameters were calculated using the CREWES Fluid Property Calculator (Ursenbach, 2009) which is based on a paper by Batzle and Wang (1992) and the Peng-Robinson (1976) equation of state.

	Brine (Fluid 1)	Dolomite (Mineral)	CO₂ (Fluid 2)
Bulk Modulus	3.3 GPa	94.9 GPa	0.081 GPa
Shear Modulus	-	45 GPa	-
Density	1112 kg/m ³	2840 kg/m ³	659 kg/m ³
Salinity	170 g/l	-	-
Viscosity	0.75 Pa.s	-	0.062 Pa.s
Initial Saturation	100%	-	0%
Final Saturation	0%	-	100%

For the seismic component of the modelling, the Zoeppritz equations (Zoeppritz, 1919; Aki and Richards, 1980) were chosen to model the offset-dependent seismogram response to the changes in the reservoir fluid properties. Synthetic seismograms were generated at 100 m increments with the maximum offset being 1500 m. The synthetic traces were normal move out (NMO) corrected and stacked to mimic the response of a post-stack seismic section. The difference between the base and monitor synthetic seismograms associated with increasing the CO₂ saturation from 0% to 100% is very subtle (Figure 38), which suggests that identifying the CO₂ plume in the Nisku Fm. will be challenging for any prospective time-lapse seismic monitoring program. The greatest change in the seismic response correlates with increasing the CO₂ saturation from 0% to 20% (Figure 39). For instance, the Ireton event shows only about a 1 ms increase in the two-way travel time (Figure 39b), most of which (~ 90%) occurs within the first 20% of CO₂ saturation in the Nisku Formation. Interesting also is the observed delay in the Nisku event travel time between the base and monitor surveys (Figure 39a). Furthermore, the Nisku event also experiences some amplitude dimming (Figure 39c); a phenomenon typically associated with class 1 and 2 amplitude variation with offset

(AVO) anomalies (Castagna, 1993). Nonetheless, the overall subtlety of the seismic response suggests that the Nisku Formation matrix is stiff and is therefore rather insensitive to fluid changes.

It is important to understand that the assumptions underlying Gassmann’s equation are not always appropriate for CO₂ fluid replacement modelling. For example, the method assumes that no interaction takes place between the fluid and the rock matrix. However, this assumption is likely to be violated due to the acidity of the CO₂, which will react with carbonate rocks. Nonetheless, the results presented here should provide an estimate of the effect of fluid replacement on the time-lapse seismic response.



CO ₂ Saturation (%)	\bar{I}_p (kg/m ² .s)	$\Delta \bar{I}_p$ (kg/m ² .s)	% Change \bar{I}_p	\bar{I}_s (kg/m ² .s)	$\Delta \bar{I}_s$ (kg/m ² .s)	% Change \bar{I}_p
0	16690486.0	0.0	0.0	9526013.3	0.0	0.0
10	16250069.4	-440416.6	-2.6	9518701.3	-7312.0	-0.1
20	16182492.3	-507993.7	-3.0	9511383.7	-14629.7	-0.2
30	16148989.8	-541496.2	-3.2	9504416.2	-21597.1	-0.2
40	16124977.4	-565508.6	-3.4	9497087.5	-28925.8	-0.3
50	16105336.2	-585149.8	-3.5	9489753.2	-36260.1	-0.4
60	16087978.5	-602507.5	-3.6	9482413.2	-43600.1	-0.5
70	16072566.9	-617919.1	-3.7	9475424.1	-50589.3	-0.5
80	16057404.0	-633082.0	-3.8	9468072.8	-57940.5	-0.6
90	16042815.7	-647670.3	-3.9	9460716.5	-65296.8	-0.7
100	16028630.8	-661855.2	-4.0	9453353.9	-72659.5	-0.8

Figure 37: Predicted changes in the average acoustic (\bar{I}_p) and shear (\bar{I}_s) impedance of the Nisku Formation as a result of increasing the CO₂ saturation from 0 to 100%. The highest incremental change is associated with increasing the CO₂ saturation from 0 to 20%. Shortly after that, the acoustic impedance reaches a plateau. The shear impedance, on the other hand, is rather insensitive to the fluid replacement.

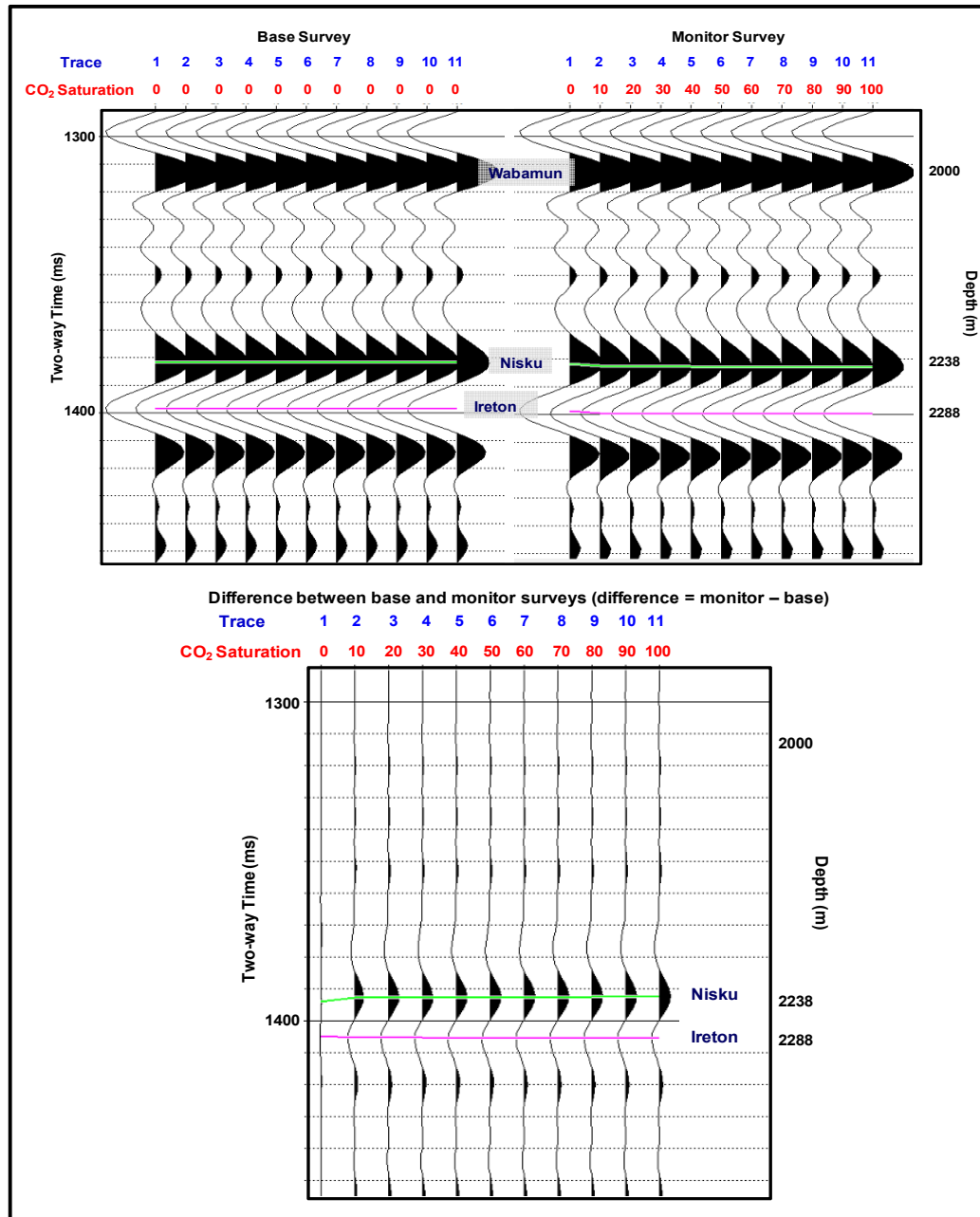


Figure 38: Top left: Offset dependent synthetic seismogram generated using the Zoeppritz equations after NMO correction and stacking; all 11 traces are identical (in the base survey) and they represent an initial condition in which the reservoir is 100% brine saturated. Top right: the same offset dependent synthetics but in this case (monitor survey) each trace has undergone a saturation transformation between brine and CO₂ as indicated by the values along the horizontal axis (red label). Bottom: the difference between the monitor and base. Changes in reservoir properties were only applied to the zone of interest, i.e., Nisku (2238 m) to Ireton (2288 m). The highest incremental change is associated with the first 10% of CO₂ saturation (trace 2). The subtle difference between the two surveys suggests that the Nisku matrix is so stiff that the fluid replacement process is only having a small effect on the observed seismic response. The modelling was undertaken using the water source well (1F1-11-29-45-2W5).

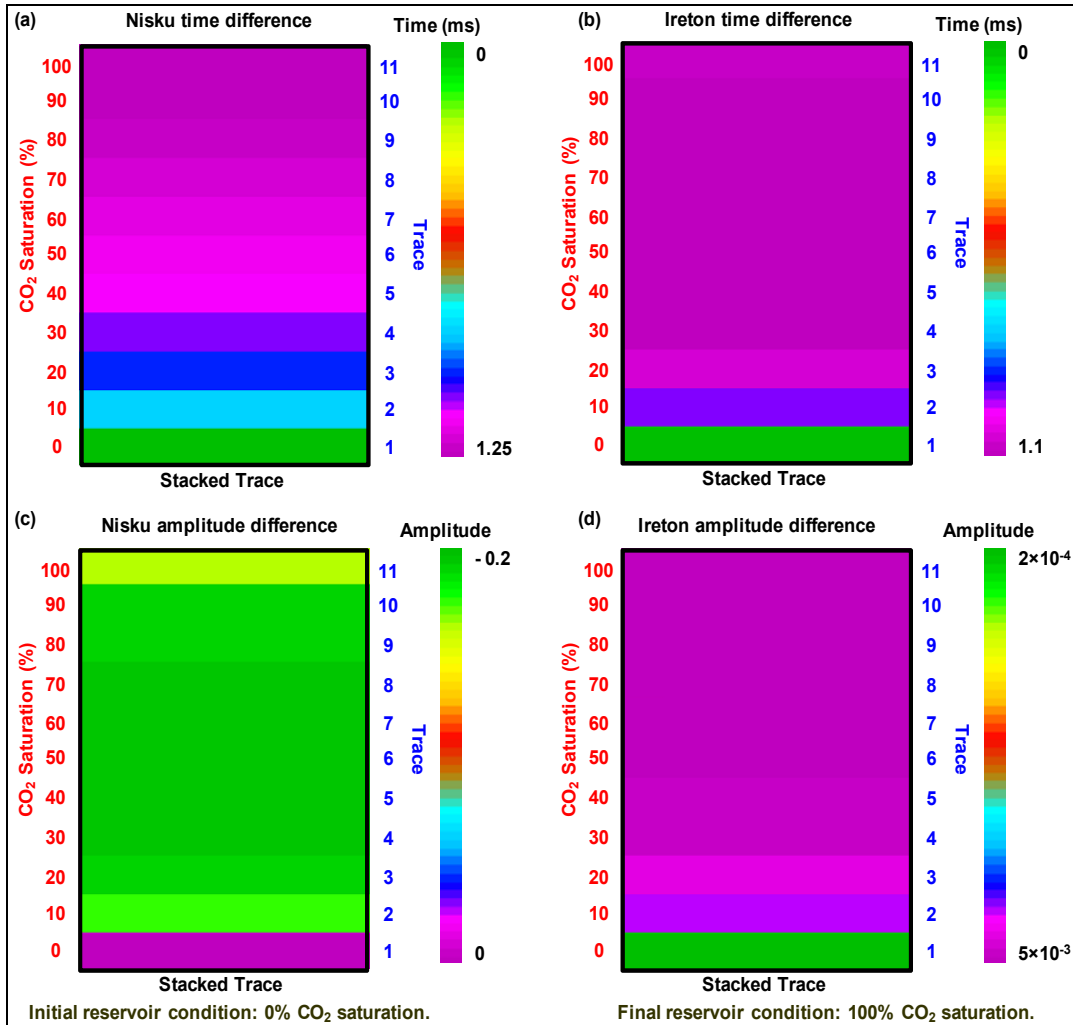


Figure 39: Mosaic display of the fluid substitution effect on the time and amplitude response of the Nisku and Ireton events, respectively, between the base and monitor surveys: (a) difference in the Nisku event two-way time (ms); (b) difference in the Ireton event two-way time (ms); (c) difference in the Nisku event amplitude; (d) difference in the Ireton event amplitude. Each horizon is obtained by subtracting the corresponding horizons between the monitor and base surveys (difference = monitor - base) in Figure 38. In all the plots the highest incremental change in time and amplitude is associated with the initial increase in CO₂ saturation (i.e., from 0 to 10%). Shortly after that, the seismic response reaches a plateau and becomes virtually unresponsive to the increase in CO₂ saturation. The modelling was undertaken using the water source well (1F1-11-29-45-2W5) shown in Figure 3.

11. CONCLUSIONS

The seismic characterization of the Nisku Formation in WASP study area has revealed two major groups of anomalies: one is associated with geological discontinuities, primarily in the overlying Wabamun Formation, while the other is interpreted to be a result of lithological/thickness changes within the Nisku Formation. In addition, regional 2D seismic lines (Figure 5, Figure 6, Figure 7, and Figure 8) were used to interpret long-wavelength geological features, the results of which indicate that there is no sign of major faulting in the study area. In comparison, detailed mapping, attribute analysis and acoustic impedance inversion were achieved using high quality 3D seismic in the northern part of the study area.

The interpreted time structure map of the Nisku Fm. (Figure 10) is rather smooth and consistent with the regional NE-SW dip orientation. The normalized root-mean squares (NRMS) amplitude map (Figure 12) shows stronger variations across the study area. Those anomalies are most likely associated with lithological variations and geological discontinuities. In order to differentiate between the two types of anomalies, seismic attributes and acoustic impedance inversion were exploited, in addition to NRMS amplitude, to delineate anomalies caused by lithological variations in contrast to those induced by geological discontinuities. Seismic amplitude modelling was undertaken to establish the principal factor affecting seismic amplitude. The modelling results (Figure 18) imply that amplitude variations in the Nisku event are caused by variations in the average P-wave velocity of the Nisku Formation driven by lithology and porosity variations. The hypothesis that lithology and porosity variations rather than thickness changes are responsible for the amplitude variations was tested against a good quality brine-bearing zone of the Nisku Formation near the southern corner of the study area. The seismic data around this water source well show significant variations in the NRMS amplitude but data from neighbouring wells suggest only a small variation in the Nisku thickness.

Seismic attributes, such as the amplitude thickness of the peak (ATP) revealed an interesting Nisku pattern that is not captured by the NRMS amplitude map. Unfortunately, there are no wells that penetrate the Nisku within that feature but, in general, by using this attribute in conjunction with the estimated bulk porosity map, we arrived at one way of identifying favourable sites. Coherency-sensitive seismic attributes, such as the difference method (Figure 24 and Figure 25), reveal numerous geologic discontinuities in the Nisku event amplitude. Even though those are interpreted to be induced by dissolution in the overlying Wabamun Formation and do not necessarily reflect physical discontinuities within the Nisku Fm. itself, they should be taken into consideration in any future CO₂ sequestration program in the area. Several favourable zones of low acoustic impedance (Figure 33) and high bulk porosity (Figure 36) are identified in the study area. However, differentiation between acoustic impedance changes caused by enhanced porosity and those associated with a possible increase in shale content remains tenuous. Finally, the fluid replacement modelling results (Figure 37 and 38) and the fact that the Nisku-Ireton is represented by one cycle in the seismic data suggest that the success of any time-lapse surface seismic program to track the CO₂ plume in the Nisku Fm will be difficult.

ACKNOWLEDGMENTS

We would like to thank the WASP sponsors and the Natural Sciences and Engineering Research Council of Canada (NSERC) for funding the project and the WASP technical team for valuable discussions, ENCANA for kindly providing access to the seismic data, and Jimmy Haszard (ENCANA), Jay LeBlanc (ENCANA), and Ian Reglar (formerly ENCANA) for providing valuable technical support. Hampson-Russell, Seismic-Micro Technology and Zokero are thanked for providing seismic interpretation software.

REFERENCES

- Aki, K., Richards, P.G., 1980. Quantitative Seismology, Freeman and Co., New York.
- Batzle, M. and Wang, Z., 1992, Seismic properties of pore fluids: *Geophysics*, 57, 1396–1408.
- Cooke, D. A., and Schneider, W. A., 1983, Generalized linear inversion of reflection seismic data: *Geophysics*, 48, 665–676.
- Gassmann, F., 1951, *Über die elastizität poroser medien: Verteljahrss-chrift der Naturforschenden Gesellschaft in Zurich*, 96, 1–23. Translated to English in the 16th issue of *Geophysics*: Gassmann, F., 1951, Elastic waves through a packing of spheres: *Geophysics*, 16, 673–23.
- Castagna, J., 1993, Petrophysical imaging using AVO: *The Leading Edge*, 12, 172.
- Ursenbach, Charles, 2009, CREWES Fluid Property Calculator Applet: <<http://www.crewes.org/ResearchLinks/ExplorerPrograms/FIProp/FluidProp.htm>>.
- Lines, L. R., and Treitel, S., 1984, A review of least-squares inversion and its application to geophysical problems: *Geophysical Prospecting*, 32, 159–186.
- Luo, Y., Higgs, W.G., and Kowalik, W.S., 1996, Edge detection and stratigraphic analysis using 3D seismic data: 66th Ann. Internat. Mtg., Soc. Expl. Geophys., Expanded Abstracts, 324–331.
- Michael, K., S. Bachu¹, B. Buschkuehle¹, K. Haug, and S. Talman, 2008, Comprehensive Characterization of a Potential Site for CO₂ Geological Storage in Central Alberta, Canada: AAPG Manuscript, 40 p.
- Peng, D.-Y. and Robinson, D. B., 1976, A New Two-Constant Equation of State: *Ind. Eng. Chem., Fundam.*, 15, 59–64.
- Russell, B.H., 1988, Introduction to seismic inversion methods: Society of Exploration Geophysicists, Course Notes Series, No. 2, S. N. Domenico, Series Editor.
- Sherriff, R. E., 1991. *Encyclopedic Dictionary of Exploration Geophysics*: Society of Exploration Geophysicists, 4th edition, Tulsa, Oklahoma.
- Smith, T. M., Sondergeld, C. H., and S. R Chandra, 2003, Gassmann fluid substitutions: A tutorial: *Geophysics*, 68, 430–440.
- Wang, Z., 2001, Fundamentals of seismic rock physics: *Geophysics*, 66, 398–412.
- Waters, K. H., 1978, *Reflection seismology*: John Wiley and Sons.
- Wylie, M. R., Gregory, A. R, and, Gardner, L. W., 1956, Elastic wave velocities in heterogeneous and porous media: *Geophysics*, 21, 41–70.
- Zoeppritz, R., 1919, On the reflection and propagation of seismic waves: *Erdbebenwellen VIII B; Göttinger Nachrichten*, I, 66–84.